Vibrational structure of crystal-field spectra in layered 3*d*-metal dihalides

I. Pollini and G. Spinolo
Gruppo Nazionale di Struttura della Materia del Consiglio Nazionale delle Ricerche, Istituto di Fisica dell'Università, via Celoria 16, 20133 Milano, Italy

G. Benedek
*Gruppo Nazionale di Struttura della Materia del Consiglio Nazionale delle Ricerche, Istituto di Fisica dell'Università, via Celoria 16, 20133 Milano, Italy**
and Max-Planck Institut für Festkörperforschung, 80 Stuttgart, Federal Republic of Germany
(Received 13 December 1979)

The vibrational structures observed in the absorption spectrum associated with the crystal-field transitions in Mn, Fe, Co, and Ni dichlorides and dibromides are studied in detail at 5 K. The choice of these crystals is motivated by their appreciable molecular character resulting in a small dispersion of optical branches and hence in the appearance of relatively sharp phonon progressions in the crystal-field spectra. Most of these phonon structures are replicas of Raman-active A_{1g} and E_g frequencies and readily interpreted in terms of many-phonon processes induced by the first-order linear electron-phonon interaction. Furthermore, in Mn and Ni dihalides some intraconfigurational transitions display interesting two-phonon progressions which are attributed to the second-order linear electron-phonon interaction. The $q = 0$ phonon frequencies of even symmetry, deduced from vibronic or Raman spectra, and those of odd symmetry, measured by far-infrared transmission, are interpreted in the framework of a deformation-dipole model. Information on the partial covalency of these compounds and on the magnitude of three-body interactions is derived.

I. INTRODUCTION

A great success of the spectroscopy of transition-metal ions was the explanation of the complex absorption structure occurring in the near infrared and visible regions in terms of transitions between *d* levels as split by the crystal field of the surrounding ions.[1] The position and the intensities of the main peaks occurring in the crystal-field spectra were in most cases easily associated with purely electronic transitions, provided that all the possible mechanisms for the splitting of *d* multiplets, such as spin-orbit interaction and low-symmetry fields, are taken into account. The existence of a ligand field, i.e., the dependence of the metal-ion electronic energy on the position of the neighbor ions, implies an important electron-phonon interaction. Several of these metal ions, either in molecules or in crystals, display static Jahn-Teller coupling.[2-4] Dynamical Jahn-Teller effects are also in evidence in the ground-state splitting of ferrous halides.[5]

Much of the fine structure actually observed in the crystal-field transitions is likely to be related to dynamical Jahn-Teller coupling. However, the most evident and primary effect of the electron-phonon coupling is represented by the multiphonon fine structure forming the various bands observed in absorption or emission spectra. Their recognition as pure phonon sidebands, rather than true Jahn-Teller induced vibronic features, is based on the observation of repetitive patterns whose spacing corresponds to some optical mode of the lattice. This procedure, well established for molecules, can be extended to crystals but not in so straightforward a fashion. Since we deal with transitions which are electric-dipole forbidden in the free ion, the basic transition with which the multiphonon sideband is associated is phonon assisted (exciton-phonon transition) or magnon assisted (exciton-magnon transition). Unlike the molecules, the phonons providing the dipole in crystals form a continuum. Thus the peak corresponding to a phonon-assisted transition has a width comparable to the dispersion of the polar phonons (the exciton dispersion being neglected).

Usually this constitutes a severe limitation to the detection of resolved phonon structures. In this respect, however, *d*-metal layered compounds represent a favorable case. Owing to their particular geometrical structure and to their partial (but still weak) covalency, the optical branches display quite a sharply peaked density of states whose width is normally less than 10% of their frequencies.[6,7] Because of such quasimolecular character, the width of the zero- (even) phonon peaks of the exciton- (odd) phonon transitions can be as small as those of the exciton-magnon transitions, namely, of only a few cm^{-1}. In this case the discrimination between the two mechanisms is based on their temperature dependence.

We have already reported some sharp phonon progressions in Mn and Ni dihalides.[8-10] The realization that this is a common feature also in Co and Fe dihalides with a layer structure, despite the complications arising from their orbitally degenerate ground state, has suggested the present, more systematic study of the vibrational structures associated with the crystal-field transitions in the dichlorides and dibromides of Mn,

Fe, Co, and Mn. These crystals, having either CdI_2 ($C6$) or $CdCl_2$ ($C19$) structure, belong to the D_{3d}^3 or D_{3d}^5 space groups, respectively, with a cation at a D_{3d} site surrounded by a slightly distorted octahedral cage of halide ions. In Sec. II we recall, as an introduction, the theory of the many-phonon structures in the absorption spectrum, making a distinction between first- and second-order processes.

Section III is devoted to the illustration of the phonon structures in the mentioned crystals. In particular, for Ni halides the recent crystal-field calculations combining the effects of spin-orbit and crystal-field perturbations[11] enable us to achieve an improved assignment of the observed absorption peaks with respect to that proposed in previous papers.[8,12]

Section IV contains a theoretical discussion of the optical frequencies deduced from the vibronic structures. Making use of the infrared transmission data, here determined for all the crystals under consideration, we perform a fitting of the experimental optical frequencies in the framework of a deformation-dipole model, where only the net charge is used as a disposable parameter. The fitting yields a reliable scale of ionicity. This is found to decrease regularly from Mn to Ni dihalides. Moreover, the residual discrepancies of the fitting show a certain regular increase from Mn to Ni, and are therefore interpreted as an effect of the increasing covalency, namely, of the three-body forces which were explicitly neglected in the present model. Along this line, some information on the two main angle-bending force constants among nearest neighbors is finally obtained.

II. SPECTRUM OF PHONON-ASSISTED TRANSITIONS

A. Absorption coefficient

We briefly recall the expression of the absorption coefficient for parity-forbidden electron transitions assisted by an odd-symmetry phonon and accompanied by sidebands of many even-symmetry phonons. For light incident along the crystal c axis (z direction), this is written as[13]

$$\alpha(\Omega)=\frac{4\pi\Omega}{\hbar\eta c V}\,\mathrm{Im}\int_{-\infty}^{+\infty}dt\,e^{i\Omega t}\langle e^{iHt/\hbar}M_x e^{-iHt/\hbar}M_x\rangle_T\,, \tag{1}$$

where Ω is the light frequency, η is the refractive index, V is the crystal volume, and M_x is the x component of the electric dipole operator. H is the one-electron Hamiltonian H_e plus the phonon Hamiltonian H_p plus the electron-phonon (e-p) interaction, namely,

$$H=H_e+H_p+\sum_{\lambda l}\frac{\partial H_e}{\partial\vec{x}_l}\vec{\psi}_{l\lambda}\left(\frac{\hbar}{2M\omega_\lambda}\right)^{1/2}(b_\lambda^\dagger e^{i\omega_\lambda t}+b_\lambda e^{-i\omega_\lambda t})$$
$$+\text{quadratic } e\text{-}p \text{ interaction}+\cdots\,, \tag{2}$$

where $\vec{x}_l$ is the position of the lth atom, and M is its mass; $\vec{\psi}_{l\lambda}$ and ω_λ are eigenvector and frequency of the λth phonon, and $b_\lambda^\dagger, b_\lambda$ are the respective creation and annihilation operators. We write the thermal average in Eq. (1) as

$$\langle\cdots\rangle_T=\left\langle\sum_i|(\Psi_g|M_x|\Psi_i)|^2\exp\left(-\frac{it}{\hbar}\Delta_{g\to i}(\Psi|H|\Psi)\right)\right\rangle, \tag{3}$$

where $|\Psi_i)=|\varphi_e,\{n_\lambda\})$ is any excited state with electronic wave function φ_e and with phonon occupation numbers n_λ, $|\Psi_g)=|\varphi_g,0)$, and $\Delta_{g\to i}$ means the difference between ith excited- and ground-state expressions. Sumi, in his theoretical investigation on exciton polarons,[14] has considered three limiting cases: nearly free excitons for weak exciton-phonon coupling, vibronic excitons with small excitation transfer, and self-trapped excitons for strong coupling. Our crystals, in agreement with their pronounced molecular character, belong to the second class, the observed phonon progressions being reminiscent of those predicted by Sumi for the small Huang-Rhys factor S (e.g., $S\leq 3$) and small exciton bandwidth ($B<1$).[14] Thus we can resort to the well-known perturbative treatment for bound-electron transitions[15] by expanding the electronic part of the exponential argument up to the second-order in the linear e-p interaction

$$-it\hbar^{-1}\Delta_{g\to e}(\varphi|H|\varphi)=-it\hbar^{-1}\Big(E_e-E_g+\sum_\gamma\hbar\omega_\gamma L_\gamma^{(1)}(b_\gamma^\dagger e^{i\omega_\gamma t}+b_\gamma e^{-i\omega_\gamma t})$$
$$+\sum_{\gamma\gamma'}\hbar(\omega_\gamma\omega_{\gamma'})^{1/2}L_{\gamma\gamma'}^{(2)}(b_\gamma^\dagger e^{i\omega_\gamma t}+b_\gamma e^{-i\omega_\gamma t})(b_{\gamma'}^\dagger e^{i\omega_{\gamma'} t}+b_{\gamma'} e^{-i\omega_{\gamma'} t})\Big), \tag{4}$$

where

$$L_\gamma^{(1)}=\left(\frac{1}{2\hbar M\omega_\gamma^3}\right)^{1/2}\Delta_{g\to e}(\varphi|\vec{\nabla}H_e\cdot\vec{\psi}_\gamma|\varphi) \tag{5}$$

and

$$L_{\gamma\gamma'}^{(2)}=\frac{1}{2M\omega_\gamma\omega_{\gamma'}}\Delta_{g\to e}\sum_k{}'\frac{1}{E-E_k}(\varphi|\vec{\nabla}H_e\cdot\vec{\psi}_\gamma|\varphi_k)$$
$$\times(\varphi_k|\vec{\nabla}H_e\cdot\vec{\psi}_{\gamma'}|\varphi) \tag{6}$$

are the first- and second-order linear e-p coupling

coefficients, respectively. E_k is any intermediate electronic level, E stands for either E_e or E_g, and $\vec{\nabla}H_e \cdot \vec{\psi}_\gamma$ is an abbreviation for $\Sigma_l (\partial H_e / \partial \vec{x}_l) \cdot \vec{\psi}_{l\gamma}$. The last term of Eq. (4) may also represent the first-order quadratic e-p contribution, provided that $L^{(2)}_{\gamma\gamma'}$ is replaced by

$$Q^{(1)}_{\gamma\gamma'} = \frac{1}{2M\omega_\gamma \omega_{\gamma'}} \Delta_{g\to l} (\varphi | \vec{\nabla}\vec{\nabla} H_e \cdot \vec{\psi}_\gamma \vec{\psi}_{\gamma'} | \varphi) . \tag{7}$$

Since we deal with non-self-trapped excitons in a perfect lattice, states φ in Eq. (5) are Bloch waves and $\vec{\psi}_\gamma$ are ground-state phonons (with γ standing for phonon wave vector $\vec{q}$ and branch symmetry). Hence, the diagonal matrix elements in Eq. (5) select $q = 0$ even-symmetry modes. For crystal-field transitions in O_h or D_{3d} symmetry, γ and γ' in Eq. (6) also refer to even modes at any $\vec{q}$, while in Eq. (7), γ and γ' are allowed to be either even or odd modes at any $\vec{q}$.

The main contribution to $L^{(2)}_{\gamma\gamma'}$ usually comes from levels φ_k close to φ, belonging to the same multiplet, and transforming according to different representations. As a consequence nontotally symmetric modes (E_g in layer structures of D_{3d} symmetry) are often involved by $L^{(2)}_{\gamma\gamma'}$. On the contrary, for the first-order quadratic term several symmetry combinations are possible in principle. A_{1g} phonons are dominant in this case, since electronic diagonal elements are involved in $Q^{(1)}_{\gamma\gamma'}$. The physical meaning of the diagonal coupling constant $Q^{(1)}_{\gamma\gamma}$ is that of an effective force-constant change for the γ phonon associated with the excited-state relaxation. Since we deal with d-d transitions, where the radial parts of φ_g and φ_e are practically the same, the relaxation is rather small. Therefore we shall disregard the first-order quadratic interaction.

As concerns the dipole matrix element of Eq. (3), we know that for crystal-field transitions in ions with inversion symmetry, the zero-phonon term $(\varphi_g | M_x | \varphi_e)$ is zero. The electric-dipole transition can then be assisted by an odd phonon ν which admixes the d levels (say φ_e) with some upper odd (p or f) level φ_u. In this case, the thermal average, Eq. (3), takes the form[16]

$$\langle \cdots \rangle_T = \sum_\nu |m_{x,\nu}|^2 [(n_\nu + 1) e^{i\omega_\nu t} + n_\nu e^{-i\omega_\nu t}] \times e^{-it(E_e - E_g + \Sigma)/\hbar} e^{-S(T)} e^{\varphi(T,t)} , \tag{8}$$

where

$$m_{x,\nu} = \left(\frac{\hbar}{2M\omega_\nu}\right)^{1/2} \frac{(\varphi_g | M_x | \varphi_u)(\varphi_u | \vec{\nabla} H_e \cdot \vec{\psi}_\nu | \varphi_e)}{E_u - E_e} \tag{9}$$

The form factor $\varphi(T,t)$ contains all the information on the phonon structure associated with the transition. The power expansion of $\exp[\varphi(T,t)]$ yields the many-phonon progressions. For first- and second-order processes, $\varphi(T,t)$ was derived by various authors in the late 1960's.[15-17] In our case ($\gamma = \gamma' = E_g$) it is

$$\varphi(T,t) = \tfrac{1}{2} \sum_\gamma |L^{(1)}_\gamma|^2 [(n_\gamma + 1) e^{i\omega_\gamma t} + n_\gamma e^{-i\omega_\gamma t}] + \tfrac{1}{32} \sum_\gamma |L^{(2)}_{\gamma\gamma}|^2 [(n_\gamma + 1)^2 e^{2i\omega_\gamma t} + n_\gamma^2 e^{-2i\omega_\gamma t}] . \tag{10}$$

Clearly, the second-order term yields two-phonon progressions ($2\omega_{E_g}$, $4\omega_{E_g}$, etc.).

The Huang-Rhys factor is defined by $S(T) = \varphi(T,0)$, while the self-energy Σ, giving the phonon-induced renormalization of the purely electronic transition energy, is expressed by

$$\Sigma = \sum_\gamma L^{(2)}_{\gamma\gamma} \hbar\omega_\gamma (2n_\gamma + 1) , \tag{11}$$

and contains only second-order contributions.

Equation (8) shows a factorization between odd phonons, assisting the electron excitation, and even phonons yielding the vibrational sidebands. Thus we speak of many-phonon structure of an exciton-phonon transition. Equation (8) formally holds also for the many-phonon structure of an exciton-magnon transition, once $m_{x,\nu}$ is reinterpreted accordingly.

B. Phonon structure of crystal-field transitions in layer crystals

The observation of several replicas of the same even-symmetry phonon and, in some case of two-phonon states, is relatively easy in layered structures because of the very small dispersion displayed by the d-d excitons as well as by the optical phonons of both even and odd symmetry. In order to discuss the various coupling schemes, we consider a $3d$-metal ion in a O_h field since trigonal distortion represents only a small perturbation in this class of layer compounds. On the contrary, the phonons strongly reflect the crystal anisotropy and have to be classified according to the irreducible representations Γ_γ of the D_{3d} point group. For the lattice modes giving phonon progressions, $\Gamma_\gamma = A_{1g}$ or E_g.

We want to discuss the e-p coupling for an intraconfigurational transition from an unmixed ground state $|\varphi_g) = |\alpha S_0 \Gamma_0, \bar{\Gamma}_0)$ of symmetry $\bar{\Gamma}_0$, belonging to the multiplet $^{2S_0+1}\Gamma_0$ of configuration $\alpha \equiv (t_2^n e^m)$, to an excited level $|\alpha S\Gamma, \bar{\Gamma})$. We assume for this level a configurational mixing (CM) with another close level $|\beta S_0 \Gamma, \bar{\Gamma})$ of different configuration $\beta = (t_2^{n\pm1} e^{m\mp1})$. When $S \neq S_0$ the CM is due to spin-orbit interaction and serves to relax the transition spin selection rule. For $S = S_0$, the CM receives a

larger contribution from the two-electron Coulomb interaction. We write the wave functions of the admixed levels as

$$|\varphi_e) = \cos\vartheta\,|\alpha S\Gamma, \bar{\Gamma}) + \sin\vartheta\,|\beta S_0\Gamma', \bar{\Gamma}), \tag{12}$$

$$|\varphi_e') = -\sin\vartheta\,|\alpha S\Gamma, \bar{\Gamma}) + \cos\vartheta\,|\beta S_0\Gamma', \bar{\Gamma}). \tag{13}$$

When only the orbital one-electron part of the linear e-p interaction is taken into account, the first- and second-order e-p coupling constants can be easily expressed in terms of matrix elements between d orbitals of e or t_2 symmetry as follows:

$$L_\gamma^{(1)} = \Delta_{g\to e}(\varphi\,|\Gamma_\gamma\,|\varphi) = d_\gamma \sin^2\vartheta + \delta_{SS_0}\sin 2\vartheta (t_2\,|\Gamma_\gamma\,|e) \tag{14}$$

and

$$L_{\gamma\gamma}^{(2)} = |(\varphi_e\,|\Gamma_\gamma\,|\varphi_e')|^2/\Delta_e = \tfrac{1}{4}|d_\gamma \sin 2\vartheta + \delta_{SS_0}\cos 2\vartheta (t_2\,|\Gamma_\gamma\,|e)|^2/\Delta_e, \tag{15}$$

where

$$d_\gamma \equiv (t_2\,|\Gamma_\gamma\,|t_2) - (e\,|\Gamma_\gamma\,|e). \tag{16}$$

Δ_e is the energy separation between the two admixed levels, and Γ_γ stands for the expression of the e-p operator of Eq. (5), which transforms like the Γ_γ irreducible representation. The amplitude of the second-order processes compared to first-order is obtained by squaring the ratio

$$\frac{L_{\gamma\gamma}^{(2)}}{L_\gamma^{(1)}} = \frac{\cos^2\vartheta}{\Delta_e}\,\frac{|d_\gamma + \delta_{SS_0}(\cot 2\vartheta)(t_2\,|\Gamma_\gamma\,|e)|^2}{d_\gamma + 2\delta_{SS_0}(\cot\vartheta)(t_2\,|\Gamma_\gamma\,|e)}. \tag{17}$$

Obviously, the smaller the CM ($\vartheta \to 0$), the larger the weight of second-order processes. When $S \neq S_0$, the minimum level separation Δ_e can be of the order of the spin-orbit constant ξ, which can be enough to give important second-order contributions, since d_γ is of the order of the crystal-field constant Dq.[1]

The phonon displacement of trigonal A_{1g} symmetry contains A_{1g} and T_{2g} symmetry coordinates of the octahedral cage, while trigonal E_g phonons contain octahedral E_g, T_{1g}, and T_{2g} coordinates. Therefore for $S \neq S_0$ both A_{1g} and E_g phonons are coupled to first and second order. However, experience shows that A_{1g} is normally dominant. When $S = S_0$ and the CM is small, the nondiagonal element $(t_2\,|\Gamma_\gamma\,|e)$ is the leading term in both first and second order e-p coupling constants. Moreover, the second-order processes become dominant, since

$$\frac{L_{\gamma\gamma}^{(2)}}{L_\gamma^{(1)}} \simeq \frac{\cos\vartheta\cot\vartheta}{4\Delta_e}(t_2\,|\Gamma_\gamma\,|e) \tag{18}$$

diverges for $\vartheta \to 0$. In practice the Coulomb CM yields rather large splittings Δ_e and, on the experimental side, we will see that only exceptionally is $L_{\gamma\gamma}^{(2)}$ much larger than $L_\gamma^{(1)}$. This is better understood later, when we shall mention the specific role of the spin-dependent ep interaction. The nondiagonal element $(t_2\,|\Gamma_\gamma\,|e)$ selects only octahedral T_{1g} and T_{2g} coordinates which have shear character symmetry. In this case the coupling with E_g phonons is dominant.

The experimental evidence of second-order progressions so far collected (see next section and Ref. 10, hereafter referred to as BPPT) shows that the occurrence of only E_g phonons is nearly a rule, and goes beyond what we would expect from the above arguments. Indeed, other possible mechanisms can carry the second-order coupling with E_g phonons, such as the trigonal distortion and the Jahn-Teller effect. The former, producing a splitting of t_2 orbitals into trigonal $e + a_1$, yields matrix elements $(a_1\,|\Gamma_\gamma\,|e)$ which exclusively involve E_g phonons, whereas the dynamical Jahn-Teller effect, also involving only E_g phonons, is known to enhance second-order e-p interaction via the mixing of the dynamically split levels.[2,18]

So far we have considered a purely orbital ep operator. However, for intraconfigurational (IC) transitions with small CM due to either spin-orbit or Coulomb interaction, a competitive mechanism of first-order coupling is the direct phonon modulation of the spin-orbit interaction within the excited- and/or ground-state multiplet.[10] This contribution vanishes only for IC transitions involving either A or E or ^1T multiplets, and this was seen to provide a simple selection rule for the occurrence of second-order progressions.

There can be an interesting intermediate case when the Coulomb configuration mixing is finite but still small enough to give first-order coupling with dominant E_g phonons. An exact superposition of one- and two-phonon progressions due to the same frequency may be observed. This would appear as an anomalous one-phonon progression with oscillating amplitudes deviating from the Poisson amplitude law $e^{-S(T)}S(T)^n/n!$ valid for weak e-p coupling [Huang-Rhys factor $S(T) < 1$]. For increasing configurational mixing, the linear e-p interaction is larger and larger and the coupling with A_{1g} phonons becomes dominant to all orders. Thus we approach gradually the case of interconfigurational transition (EC) $(t_2^n e^m \to t_2^{n-k} e^{m+k})$.

For EC transitions the orbital ep interaction reduces to terms like $k[(e\,|H_{e\text{-}p}\,|e) - (t_2\,|H_{e\text{-}p}\,|t_2)]$, which are always nonvanishing for coupling with A_{1g} phonons. Such a coupling term, of the order of kDq, is several times $\omega_{A_{1g}}$, and yields broad bands with possible *weak* A_{1g} phonon structure oscillations at the low-energy side.

III. EXPERIMENTAL VIBRONIC SPECTRA

A. Experimental techniques

All the crystals were grown by the flow-system method with the halogen gas carried by dry nitrogen and attacking the powdered metal at a temperature typical for each crystal. The crystals so obtained were chosen while standing on a hot plate to prevent rapid deterioration due to moisture. With the exception of Ni halides, all the crystals are highly hygroscopic. Platelets of greater size and higher optical quality were used for absorption measurements, whereas second-choice crystals were used to prepare the samples for the far-infrared absorption.

Moisture gave major problems in the far infrared, but pellets almost free of moisture were prepared by pouring polyethylene powder in a hot mold containing the powdered crystals and stirring until the whole was fluid and well mixed. After cooling a disk 25 mm in diameter, ~1 mm thick, and ~250 mg in weight was obtained with crystal concentration ranging from 2% to 5%. The quality of the pellets from the point of view of moisture content was judged by taking a medium-infrared spectrum in which particularly prominent is the 1595-cm^{-1} band associated with the bending of the OH bond.

Far-infrared absorption spectra, presented and discussed at the end of this section, were recorded in the range 50–400 cm^{-1} using a FIS-3, Perkin Elmer grating double-beam ratio-recording spectrophotometer. In the medium infrared, the instrument used was a Perkin Elmer 180 spectrophotometer. Visible absorption spectra were taken in a liquid-helium cryostat which, for temperature-dependence studies, was allowed to warm up slowly. The temperature was checked by a CLTS sensor by Oxford Instruments; absolute error was evaluated as ±1 K. The spectrophotometer was a double-beam Cary 14.

B. $MnCl_2$ and $MnBr_2$

The optical absorption spectra of layer Mn dihalides were reported by several authors both at 78 K (Refs. 19–23) and at 5 K.[20,9] Our general crystal-field spectra of $MnCl_2$ and $MnBr_2$ at 80 and 4.2 K are reported in Figs. 1 and 2, respectively. All the bands are spin forbidden and the attributions are indicated following the calculation given by Orgel[24] in the weak crystal-field approximation. In the present analysis, however, we found it more convenient to refer to the recent ligand-field diagrams reported by König and Kremer[11] for vanishing spin-orbit coupling but including the effect of various axial fields. Hereafter the guideline for the interpretation of the vibronic structures is given by the experimental Raman frequencies of A_{1g} and E_g symmetry listed in Tables I (dichlorides) and II (dibromides).[10,25] In the following list only the transitions from the ground sextet $^6A_1(e^2t_2^3)$ to the excited quartets have been taken into account as the doublets should have a negligible oscillator strength.

$^4T_1(G)$ and $^4T_2(G)$. These are EC transitions ($k=-1$) and give broad bands where only a weak A_{1g}

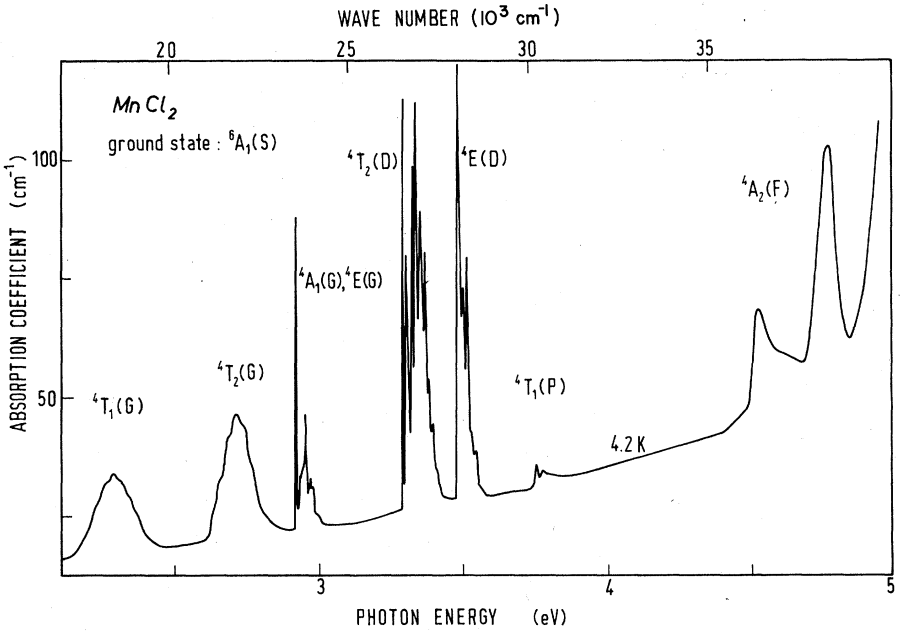

FIG. 1. Crystal-field spectrum of $MnCl_2$ at 4.2 K.

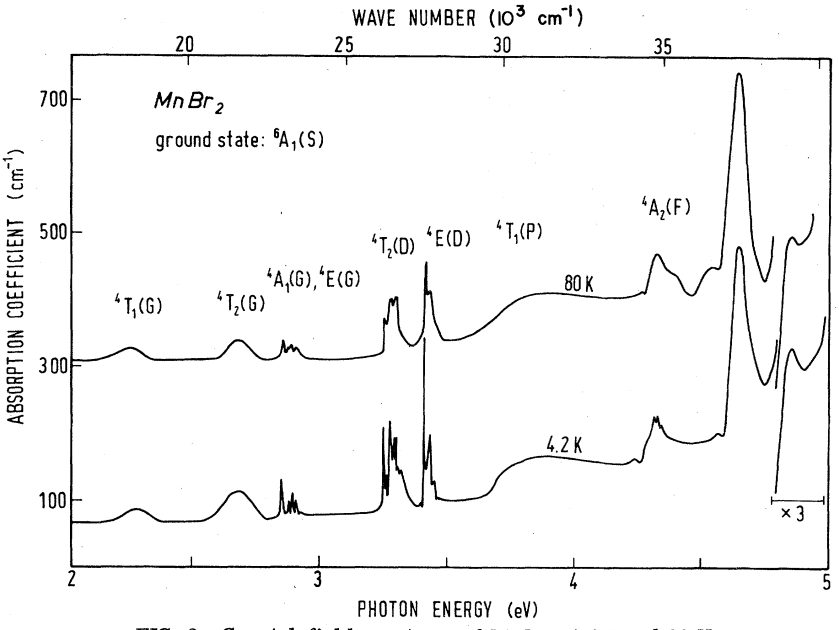

FIG. 2. Crystal-field spectrum of $MnBr_2$ at 4.2 and 80 K.

structure is visible. The structure is observed only in $MnCl_2$, however, and is more evident in $^4T_2(G)$ (Fig. 3) because of the appreciable CM with the above $^4T_2(D)$, which slightly reduces the *ep* interaction. The band $^4T_1(G)$ has been thoroughly investigated in MnF_2 because of the sharp features appearing below the Néel temperature T_N and associated with magnon-assisted transitions.[26] In $MnCl_2$ and $MnBr_2$, having a much lower T_N, nothing similar was detected.

$^4E(G)$ and $^4A_1(G)$. The transitions to these quasi-degenerate levels are quite interesting because of

TABLE I. Coulomb, dipolar, second-neighbor, and van der Waals force constants and calculated and experimental frequencies for different symmetries in 3*d*-metal dichlorides.

	Γ_γ	ϕ_C	ϕ_d	ϕ_{2n} (kg s^{-1})	ϕ_{vdW}	ω_γ (cm^{-1}) calc.	vibronic	Raman, ir
$MnCl_2$	A_{1g}	7.315	4.051	31.631	−7.966	202	228 ± 5	234
	E_g	−8.412	−2.026	4.473	−0.613	145	133 ± 8	144
	A_{2u}	7.741	15.321			284		255
	E_u	−10.953	−7.661			188		185
$FeCl_2$	A_{1g}	5.384	2.741	43.291	−10.083	211	228 ± 8	248
	E_g	−6.676	−1.371	5.974	−0.776	152	137 ± 8	145
	A_{2u}	5.681	12.576			275		270
	E_u	−8.826	−6.288			199		192
$CoCl_2$	A_{1g}	5.216	2.560	47.970	−10.907	247	254 ± 9	250
	E_g	−6.645	−1.280	6.564	−0.839	145	148 ± 8	151
	A_{2u}	5.453	12.544			282		270
	E_u	−8.943	−6.273			214		206
$NiCl_2$	A_{1g}	5.134	2.520	48.111	−10.932	230	261 ± 3	269
	E_g	−6.552	−1.260	−6.585	−0.841	176	160 ± 7	173
	A_{2u}	5.335	12.375			297		293
	E_u	−8.924	−6.187			234		225

TABLE II. Coulomb, dipolar, second-neighbor, and van der Waals force constants, and calculated and experimental frequencies for different symmetries in 3*d*-metal dibromides.

	Γ_γ	ϕ_C	ϕ_d	ϕ_{2n}	ϕ_{vdW}	ω_γ (cm^{-1}) calc.	vibronic	Raman, ir
			($kg\ s^{-1}$)					
$MnBr_2$	A_{1g}	5.919	2.447	45.309	−10.184	137	151 ± 5	151
	E_g	−8.358	−1.224	6.588	−0.784	93	93 ± 9	90
	A_{2u}	6.680	15.812			235		234
	E_u	−11.232	−7.906			145		143
$FeBr_2$	A_{1g}	6.358	2.404	52.161	−11.268	147	155 ± 5	157
	E_g	−9.330	−1.202	7.511	−0.887	99	98 ± 5	93
	A_{2u}	6.712	17.616			246		231
	E_u	−12.645	−8.808			163		154
$CoBr_2$	A_{1g}	4.006	1.373	59.348	−12.377	157	152 ± 6	162
	E_g	−6.115	−0.744	8.469	−0.952	93	105 ± 7	98
	A_{2u}	4.197	11.498			224		230
	E_u	−8.467	−5.749			163		161
$NiBr_2$	A_{1g}	3.007	0.979	62.934	−12.921	152	167 ± 4	168
	E_g	−4.677	−0.480	8.942	−0.994	110	95 ± 5	105
	A_{2u}	3.131	8.777			235		230
	E_u	−6.591	−4.389			191		181

their IC character [Figs. 4(a) and 5(a)]. The degeneracy predicted in the cubic approximation is removed by the trigonal field.[11] The phonon structures should then begin from two different origins. Indeed in $MnBr_2$ some progressions start around 23 080 cm^{-1}, while another progression begins at 23 380 cm^{-1} with a splitting of 300 cm^{-1}. Analogous behavior was found in MnI_2,[19] while the situation in $MnCl_2$ is less clear. The fact that trigonal perturbation in other crystals of this class is comparable to spin-orbit coupling[5] could explain such a large splitting. On the other hand, the first two unresolved peaks of the structure, having a separation of nearly 40 cm^{-1} in all MnX_2, are more likely to be the Jahn-Teller doublet of $^4E(G)$ rather than the

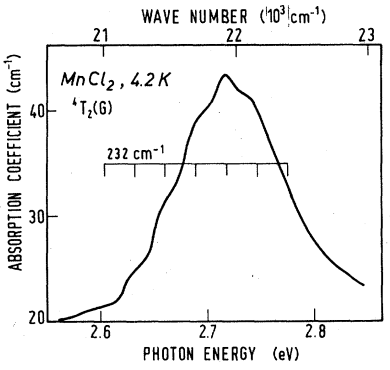

FIG. 3. $^4T_2(G)$ band of $MnCl_2$ at 4.2 K.

origins of $^4E(G)$ and $^4A_1(G)$ progressions. Uniaxial stress experiments could clarify this point. As concerns phonons, we note that the IC nature of this level, with only a very small configurational mixing, should cause the superposition of important two-phonon series. In this case it would be easier to account for the complicated observed structure. Since the representation Γ_8 is contained twice in $^4E + {}^4A_1$, one predicts also an $A_{1g} \times A_{1g}$ progression, but this is not evident in Figs. 4(a) and 5(a). Instead for E_g the strong two-phonon character appears in MnI_2; the progression of 140 cm^{-1}, reported by van Erk,[19] is further evidence of a pure $E_g \times E_g$ progression, ω_{E_g} being in layer 3*d*-metal iodides around 70 cm^{-1}.[27]

$^4T_2(D)$. Because of the exceptionally strong CM with $^4T_2(G)$, this transition has a partial IC character and a weaker *e*-*p* coupling. Therefore nice A_{1g} phonon progressions, extending up to the fifth order, appear in both crystals [Figs. 4(b) and 5(b)]. In $MnBr_2$, three progressions, with separations of the origins of 45 and 25 cm^{-1}, are well resolved, while in $MnCl_2$ the second and third series are presumably too close to be distinguishable. Such a splitting could be attributed to the combined effect of spin-orbit and trigonal perturbations.

$^4E(D)$. The strong IC character of $^4E(D)$ is only weakly perturbed by spin-orbit mixing at the crossing with the $^4T_1(P, e^3t_2^2)$ level. Thus it exhibits an A_{1g} progression, which is characterized by quite a weak *e*-*p* interaction, namely, by a

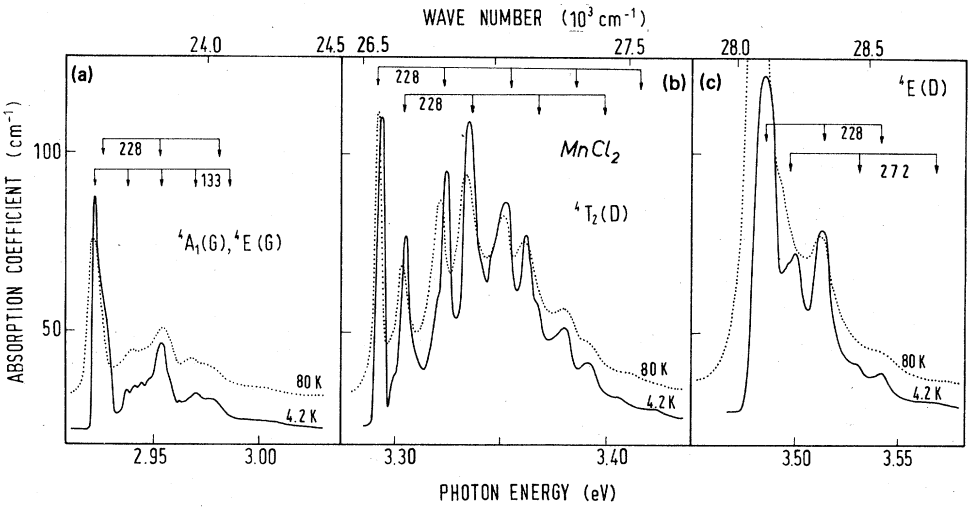

FIG. 4. $^4A_1(G)$, $^4E(G)$, $^4T_2(D)$, and $^4E(D)$ bands of $MnCl_2$ at 4.2 and 80 K.

rapid intensity decrease with increasing phonon order. The weaker intercalated progression observed in $MnCl_2$ cannot be assigned to A_{1g} mode, the spacing being quite a bit larger (~272 cm^{-1}). Since the theory also predicts no spin-dependent e-p interaction for this transition, the second progression is interpreted as a second-order $E_g \times E_g$ (whose spacing should be 266 cm^{-1}).

$^4T_1(P)$ and $^4A_2(F)$. The former displays some structure only in $MnCl_2$, which, by the way, does not seem to have a phonon origin. On the other hand the $^4T_1(P)$ of $MnBr_2$ is a broad band, in agreement with its EC nature. On the contrary, $^4A_2(F)$ is IC to a good extent, despite the numerous crossings with doublet levels of et_2^4 configuration. In $MnBr_2$, it gives a single weak progression (Fig. 6) with a spacing of ~140 cm^{-1}. This is quite a bit smaller than the Raman A_{1g} frequency (151 cm^{-1}). However, the experimental uncertainty is large in this case, and we cannot exclude just an excited-state relaxation effect.

In principle, all the frequencies associated with the above transitions should be slightly different and shifted with respect to the Raman frequencies, due to the different relaxation of the excited states. If we except the case of $^4A_2(F)$, however, such a shift is often very small and within the experimental error. Therefore the vibronic frequencies collected in Tables I and II with the corresponding errors are obtained from averaging over all the transitions.

C. $FeCl_2$ and $FeBr_2$

Accurate investigations of crystal-field transitions from the ground quintet $^5T_2(D, e^2t_2^4)$ and of the magnetic properties of iron dihalides appeared recently.[28-30] From crystal-field diagrams calculated by König and Kremer (KK) including spin-orbit interaction[31] ($\xi = 420$ cm^{-1}), but not trigonal distortion (which, for simplicity, here is also neglected in spite of some recent evidence in-

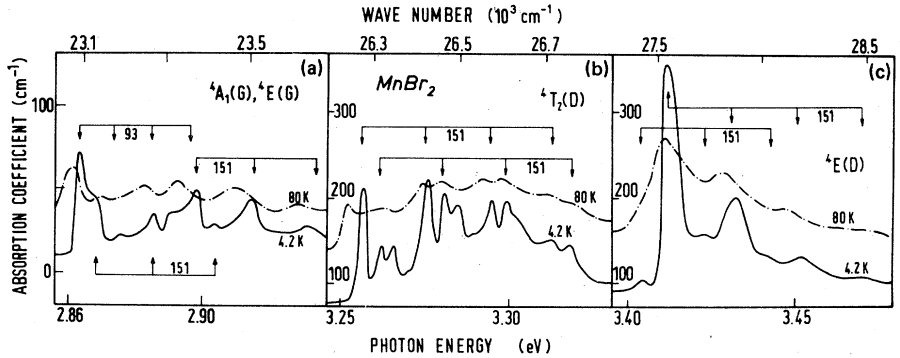

FIG. 5. $^4A_1(G)$, $^4E(G)$, $^4T_2(D)$, and $^4E(D)$ bands of $MnBr_2$ at 4.2 and 80 K.

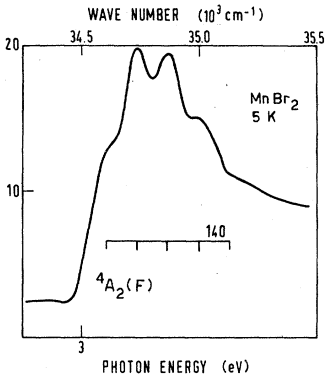

FIG. 6. $^4A_2(F)$ band of $MnBr_2$ at 5 K.

dicating an appreciable trigonal-field effect on the ground-state multiplet[5]), a reasonable fit of the Frank-Condon peaks is obtained with $Dq = 600$ cm^{-1} for $FeBr_2$.[28] Here the best adjustment of the origins of the various phonon progressions is obtained from those calculations with $Dq = 600$ cm^{-1} for $FeCl_2$ and 550 cm^{-1} for $FeBr_2$. Our general spectra are shown in Figs. 7 and 8.

$^5E(D)$, $^3T_1(H)$, and $^3T_2(H)$. These are EC transitions ($k = 1$ for the first, $k = -1$ the other two) and display no resolved structure, except $^5E(D)$ which exhibits a double-peak feature, presumably due to Jahn-Teller effect.[28]

$^3T_1(H) + {}^1A_1(I)$. The first level is IC and would be a candidate for a well-resolved phonon structure, while $^1A_1$ is EC with $k = -2$, and is strongly forbidden by configurational and spin ($\Delta S = -2$) selection rules. But the two levels cross each other with an appreciable spin-orbit mixing just at $Dq = 500$ cm^{-1}. The weak Γ_1-component mixing of $^3T_1$ with this highly EC level is probably sufficient to enhance greatly the e-p coupling, giving a broad band. Moreover there is also a strong Γ_4-component spin-orbit mixing with $^1T_1(I)$. On the other hand, the remaining Γ_3 and Γ_5 components of $^3T_1(H)$ are practically unperturbed and without any appreciable phonon-induced mixing, since $\Gamma_3 \times \Gamma_5$ does not contain A_{1g} or E_g. Indeed, no one-phonon or two-phonon resolved series are found in the $^3T_1 + {}^1A_1$ band.

$^3T_2(F) + {}^3E(H) + {}^3T_1(P) + {}^1T_1(I)$. In the region $Dq = 500$ to 600 cm^{-1} these levels are quite close to each other, the reciprocal distances being of the order of the spin-orbit interaction. It is convenient to consider these terms altogether as a spin-orbit split giant multiplet, whose levels at $Dq = 600$ cm^{-1} are, in ascending order,[31] $\Gamma_4(^3T_2)$, $\Gamma_3(^3T_2)$, $\Gamma_5(^3T_2)$, $\Gamma_2(^3T_2)$, $\Gamma_5(^3E)$, $\Gamma_4(^3T_1)$, $\Gamma_5(^3T_1)$, $\Gamma_3(^3T_1)$, $\Gamma_4(^3E)$, $\Gamma_1(^1T_1)$, and $\Gamma_1(^3T_1)$. The splittings, as derived from the KK calculations,[31] for a spin-orbit constant $\xi = 420$ cm^{-1} are shown in Fig. 9. The comparison of this level distribution with the positions of the main peaks observed in $FeCl_2$ [Figs. 10 and 9(a)], from where the phonon series are argued to start, show a surprising agreement, except for a scale factor: The experimental structure of these levels is 1.5 times more spread in energy. An analogous situation is found for the experimental structure of $FeBr_2$ when compared with the calculation for $Dq = 550$ cm^{-1} [Fig. 11 and Fig. 9(b)]. Perhaps a larger ξ or the inclusion of tri-

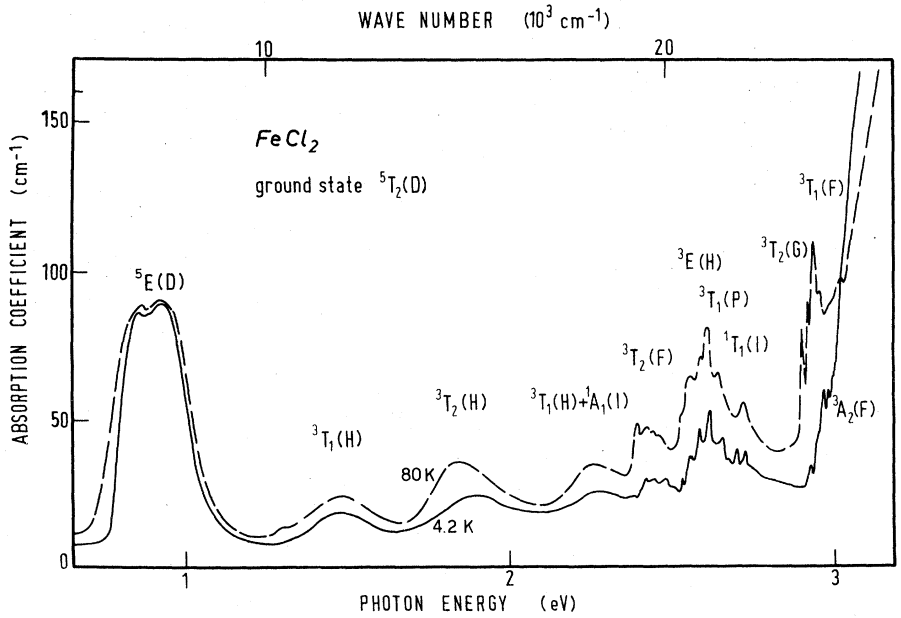

FIG. 7. Crystal-field spectrum of $FeCl_2$ at 4.2 and 80 K.

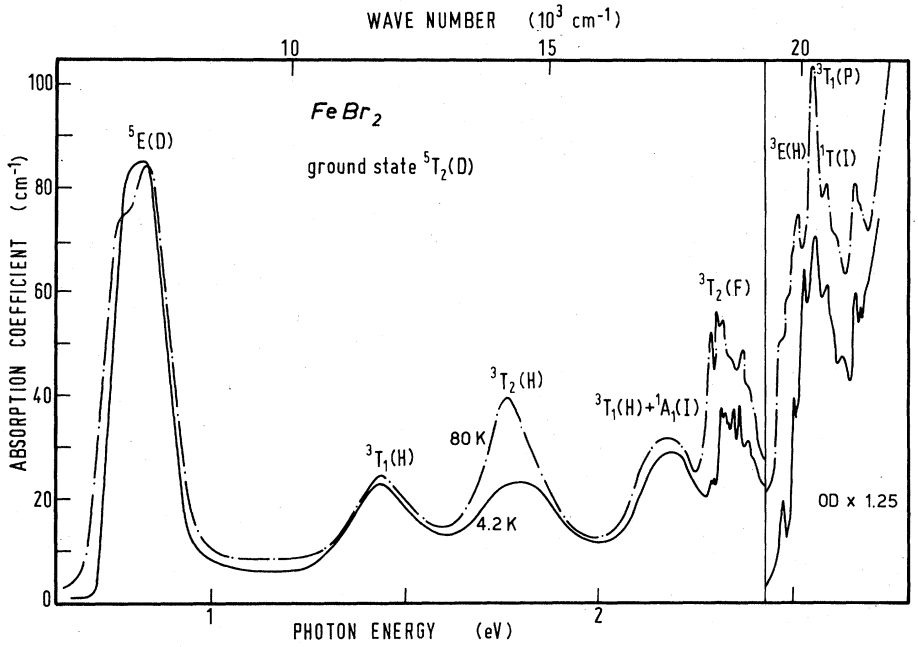

FIG. 8. Crystal-field spectrum of $FeBr_2$ at 4.2 and 80 K.

gonal-field effects could remove this discrepancy. Nevertheless, this scheme supplies a useful basis for discussing the phonon coupling to all these transitions.

The rich phonon structure of these levels is quite expected due to their predominant IC nature. Also $^1T_1(I)$, which is EC with $k=-1$, has a relevant IC character at $Dq \sim 600$ cm^{-1} because of the strong spin-orbit mixing (which, on the other hand, makes this level observable) with the other levels, while $^3E(H)$ displays an important CM with the upper $^3E(P)$ ($\Delta k=+1$). It follows that levels of Γ_5 symmetry have a larger CM ($\Delta k=+1$) via the mixing of ^3E terms, while Γ_4 levels have a larger CM ($\Delta k=-1$) via the spin-orbit coupling with $^1T_1$. König and Kremer diagrams show the exception of $\Gamma_4(^3E)$ which is weakly dependent on Dq because of cancellation of the two opposite CM's. Therefore, E_g phonon structures should be preferably associated with Γ_1, Γ_2, Γ_3 and $\Gamma_4(^3E)$ levels, which have a weak CM while A_{1g} phonons should be dominant with the other Γ_4 and Γ_5 levels. This is well consistent with what is seen in $FeBr_2$ and gives a key for interpreting several of the structures observed in $FeCl_2$. Clearly this discussion covers only one aspect of the complex phenomenology, as recent experiments[28-30] show that some of the fine structure could be related to exchange splitting and magnetic excitations.

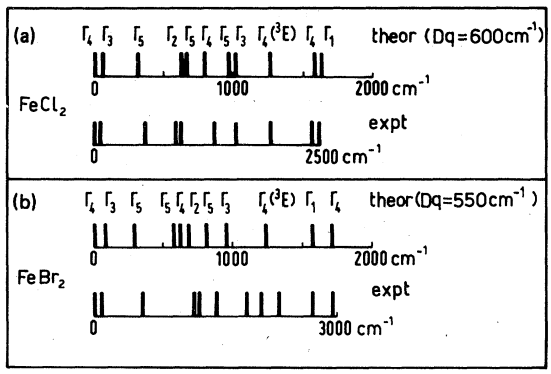

FIG. 9. Theoretical and experimental sequences of levels within the $^3T_2(F)+{}^3E(H)+{}^3T_1(P)+{}^1T_1(I)$ admixed multiplets in $FeCl_2$ and $FeBr_2$.

$^3T_2(G)+{}^3T_1(F)+{}^3A_2(F)+{}^1T_2(I)$. In $FeCl_2$ the IC transition to $^3T_2(G)$ is also observed. From KK calculations the spin-orbit splitting of this level yields the narrow quartet of levels Γ_5, Γ_3, Γ_2, and Γ_4. Owing to the modest CM with $^3T_2(F)$, the quartet, which is identified with the structure at 23 500 cm^{-1}, is the origin of four E_g progressions and, at least, one A_{1g} progression. Just 600 cm^{-1} above the $^3T_2(G)$ quartet, the KK calculation predicts the levels $\Gamma_5[^3T_1(F)]$ and $\Gamma_5[^3A_2(F)]$, both EC with $k=1$ and strongly hybridized with the $\Gamma_5[^3T_2(G)]$ ($k=0$) and the $\Gamma_5[^1T_2(I)]$ ($k=-1$) and, obviously, each with the other. The effect of such a complex mixing is apparent in the KK diagram: The slope of both Γ_5 levels with respect to Dq is

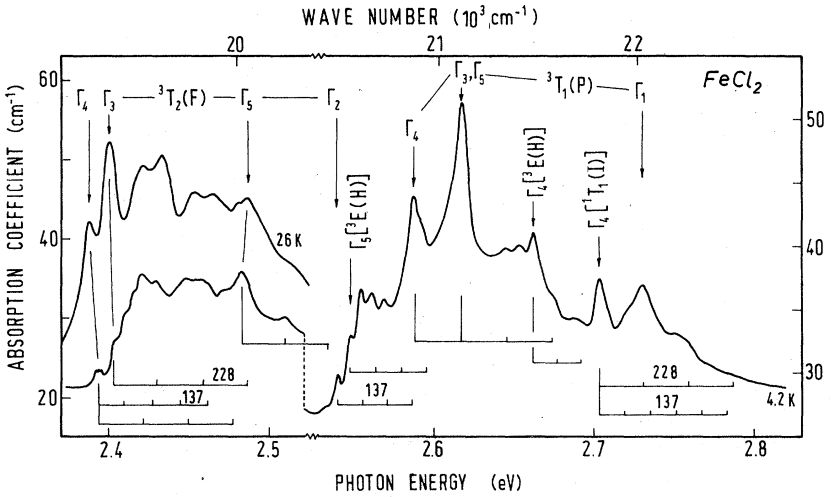

FIG. 10. $^3T_2(F)+{}^3E(H)+{}^3T_1(P)+{}^1T_1(I)$ bands of $FeCl_2$ at 4.2 and 26 K.

quite reduced in comparison with what is expected for $k=1$ EC levels. As a consequence two A_{1g} progressions are observed. (See Fig. 12.) The vibronic frequencies of $FeCl_2$ and $FeBr_2$, averaged on all the observed progressions, are reported in Tables I and II, respectively.

D. $CoCl_2$ and $CoBr_2$

Crystal-field spectra of $CoCl_2$ and $CoBr_2$ were studied experimentally as early as 1963 by Ferguson, Wood, and Knox,[32] and reasonably fit in the cubic-field approximation with $Dq=690$ cm^{-1}, $B=780$ cm^{-1}, $C/B=4.40$, $\xi=420$ cm^{-1} for $CoCl_2$ and $Dq=640$ cm^{-1}, $B=760$ cm^{-1}, $C/B=4.40$, $\xi=420$ cm^{-1} for $CoBr_2$. Energy-level calculations including spin-orbit interaction ($\xi=450$ cm^{-1}) have been reported by Liehr[33] and are used in the present discussion. The ground multiplet is $^4T_1(F, e^2t_2)$, and is split by spin-orbit interaction to give a ground doublet of Γ_6 symmetry. The general crystal-field spectra are reported in Fig. 13. and Fig. 14. The lowest crystal-field transitions, to $^4T_2(F)$, $^2E(G)$, and $^4A_2(F)$ are all EC: No resolved vibronic structure is observed.

$^2T_1(G)$ and $^2T_2(G)$. These two weak spin-forbidden IC transitions present in both crystals very weak phonon structures in the higher-energy side (Figs. 15 and 16). One or perhaps two progressions with a single frequency close to A_{1g} Raman frequency (Tables I and II) can be recognized. We need to associate these progressions with the components Γ_6 of $^2T_1$ and Γ_7 of $^2T_2$, since these levels present only a very weak CM via the spin-orbit interaction with Γ_6 and Γ_7 of the above $^4T_1(P)$, while the other two components Γ_8 due to the mixing with Γ_8 of $^4A_2(F)$ loose much of their IC character and do not show any appreciable structure but only broad bumps.

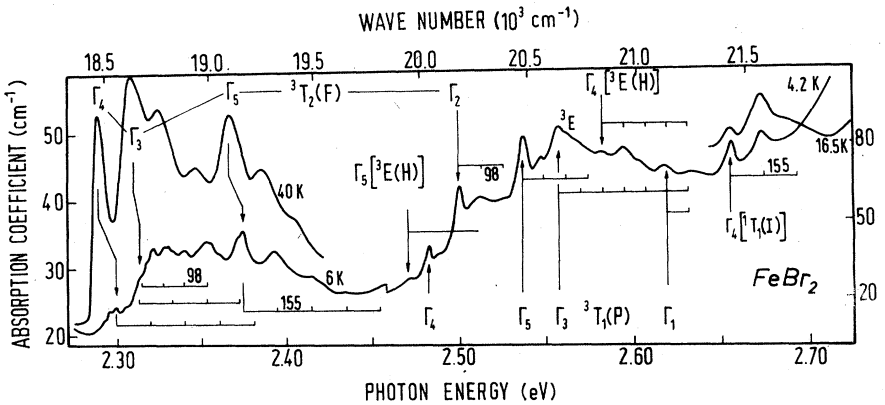

FIG. 11. $^3T_2(F)+{}^3E(H)+{}^3T_1(P)+{}^1T_1(I)$ bands of $FeBr_2$ at various temperatures.

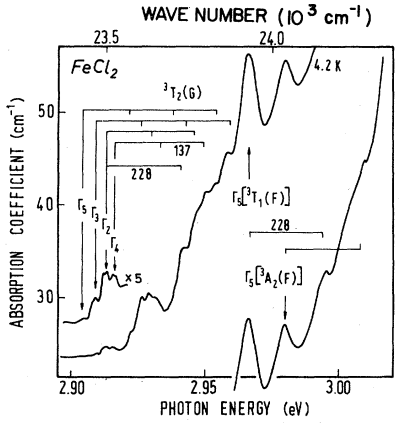

FIG. 12. $^3T_2(G)+{}^3T_1(F)+{}^3A_2(F)$ bands of $FeCl_2$ at 4.2 K.

$^4T_1(P)$. This spin-allowed transition gives the most prominent feature among all Co^{2+} crystal-field absorption bands. However, because of the CM with the ground multiplet and the spin-orbit coupling of the Γ_6 and Γ_8 components with the respective components of the above $^2T_1(P, e^2t_2)$, the EC character of this transition is attenuated. Thus the three spin-orbit components $\Gamma_7+\Gamma_8$, Γ_8, and Γ_6 can be distinguished, and also weak oscillations due to vibronic progressions are argued. In $CoCl_2$, where these oscillations are better seen by means of the second-order derivative of the band shape (Fig. 17), a single frequency, close to that of A_{1g} Raman mode (250 cm^{-1}), accounts for all the observed features. In $CoBr_2$, only the shoulder of the $^4T_1(P)$ band, assigned to Γ_6, exhibits a well-resolved phonon structure [Fig. 18(a)], and this consists of two close progressions with the same spacing of 105 cm^{-1}, fairly close to the Raman E_g frequency.

$^2A_1(G)+{}^2T_1(P)$. In the region around $Dq=700$ cm^{-1} the Γ_6 component of these two levels are strongly hybridized, while the Γ_8 component of $^2T_1(P)$ contains some percentage of $\Gamma_8[^4T_1(P)]$. Since $^2T_1(P)$ is IC, some resolved phonon progressions are observed [Figs. 18(b) and 19]. In both crystals, the three progression origins associated with the above spin-orbit components can be located for $CoCl_2$ at the small peak at 18 822 cm^{-1} (Γ_6) and at the two sharpest peaks at 19 044 (Γ_8) and 19 806 cm^{-1} (Γ_6). The same assignment is made in $CoBr_2$, where analogous structures exist at 17 662, 17 825, and 18 594 cm^{-1}, respectively. In $CoCl_2$, the two Γ_6 origins reveal a fine structure, namely, a doublet with separations of 7 cm^{-1} and 55 cm^{-1}, while in $CoBr_2$ this structure is not resolved.

The fitting by means of progressions with spacing equal to A_{1g} or E_g Raman frequencies (Tables I and II) give only a partial account of the observed structures. Clearly the upper Γ_6 progression in both crystals and the Γ_8 progression of $CoBr_2$ require an intermediate phonon frequency: 177 cm^{-1} for $CoCl_2$ and 133 cm^{-1} for $CoBr_2$. These frequencies are some 30 cm^{-1} larger than the respective E_g frequencies and can be hardly ex-

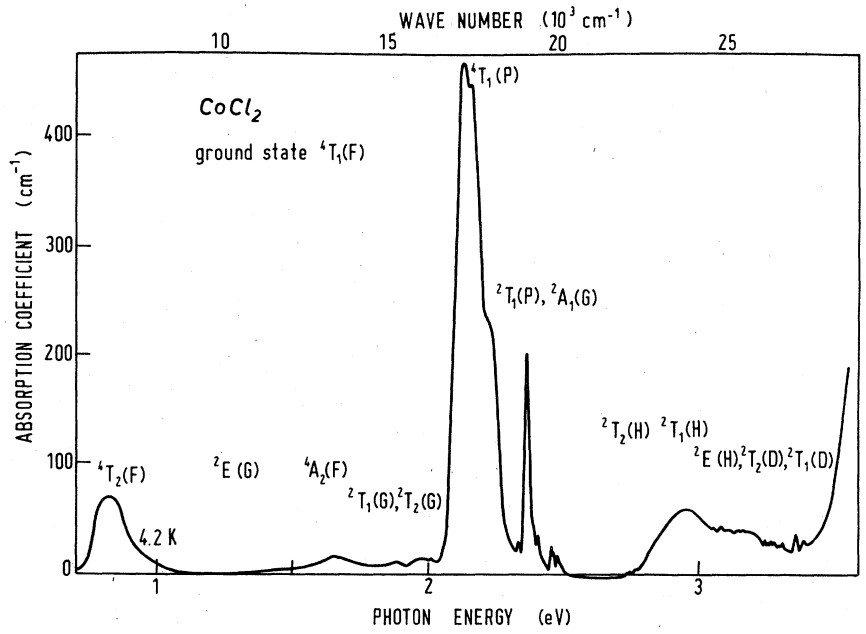

FIG. 13. Crystal-field spectrum of $CoCl_2$ at 4.2 K.

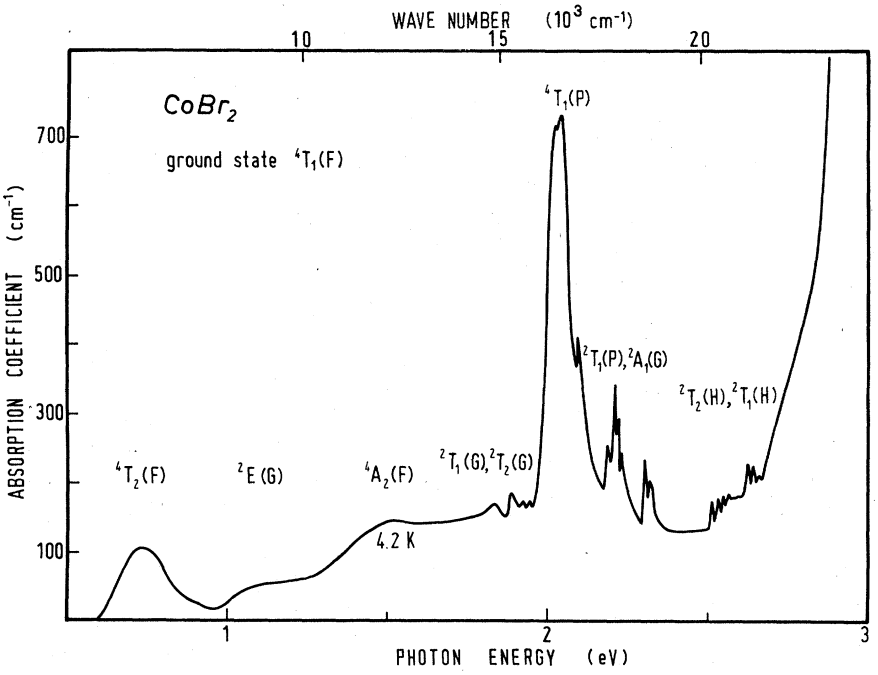

FIG. 14. Crystal-field spectrum of $CoBr_2$ at 4.2 K.

plained in terms of an excited-state relaxation. Also the dynamical Jahn-Teller mechanism cannot account for such a large renormalization of the E_g phonon frequency, since no diagonal coupling exists for Γ_6 states.

$^2T_2(H) + {}^2T_1(H)$. The transitions to these two levels, admixed through their Γ_8 components, show a rather complex vibronic structure. However, some progressions are identified in both crystals (Figs. 20 and 21). The slope of $^2T_2(H)$ vs Dq is appreciable, in spite of its IC nature, owing to CM. Therefore the phonon structure is weak (particularly in $CoCl_2$) and reveals only A_{1g} phonons. The third progression in $CoBr_2$ is mainly associated with $^2T_1$ (which is EC with $k=1$) and is the starting point of a band completely covered by the charge-transfer edge. In $CoCl_2$, the peak around 22150 cm^{-1} seems to be also the origin of another A_{1g} progression (or of an E_g progression with $\omega_{E_g} \sim 150$ cm^{-1}). In $CoBr_2$, the separation of the three spin-orbit components of about 460 cm^{-1} is consistent with Liehr's calculations for a spin-orbit constant $\xi = -450$ cm^{-1} and $Dq = 600$ cm^{-1}.[33] In $CoCl_2$, such a separation is somewhat smaller. It seems unlikely that the possible progressions starting from 22150 cm^{-1} be associated with $^2T_1(H)$. Rather the IC $^2T_1(H)$ transition should be related with the wide bump at 23900 cm^{-1} (Fig. 22).

$^2E(H)$, $^2T_2(D)$, and $^2T_1(D)$. In $CoCl_2$ these transitions are observable and reveal some nice progressions of the A_{1g} phonon (Fig. 22). This is not completely expected, as these EC levels present

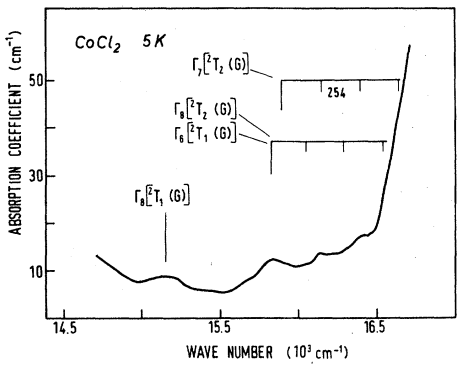

FIG. 15. $^2T_1(G) + {}^2T_2(G)$ bands of $CoCl_2$ at 5 K.

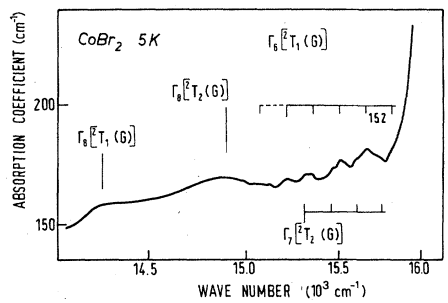

FIG. 16. $^2T_1(G) + {}^2T_2(G)$ bands of $CoBr_2$ at 5 K.

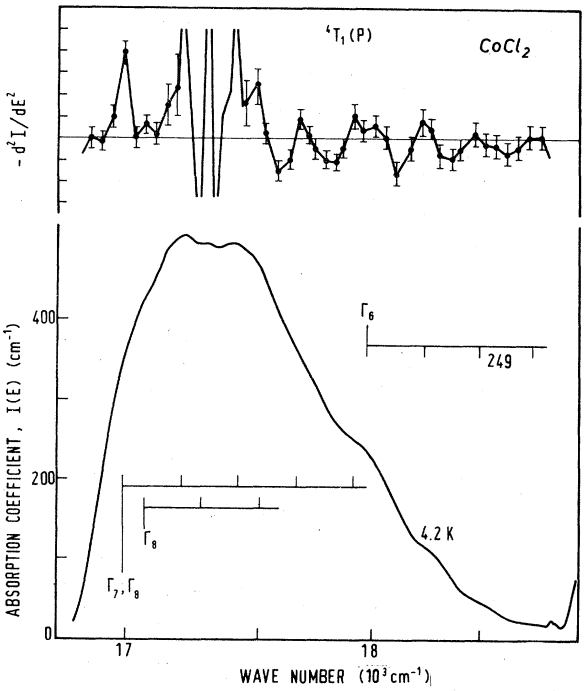

FIG. 17. $^4T_1(P)$ band of $CoCl_2$ with the second-order derivative at 4.2 K.

only quite a weak CM with levels of e^2t_2 configuration. While the disentangling of $^2E(H)$ and $^2T_2(D)$ vibronic spectra is rather complicated (three or four series, at least, are needed), the two progressions Γ_6 and Γ_8 of $^2T_1(D)$ are surprisingly sharp and simple, allowing for a relatively precise determination of the spacing. The vibronic frequencies derived from the average over all the observed progressions (except those of $\Gamma_6[^2T_1(P) + {}^2A_1(G)]$) are listed in Tables I and II.

E. $NiCl_2$ and $NiBr_2$

Kozielski and two of us reported in 1972 a detailed study of crystal-field transitions in $NiCl_2$ and $NiBr_2$.[8] The assignment of the observed spin-forbidden transitions within an octahedral crystal-field scheme including spin-orbit interaction,[34] but neglecting trigonal-field distortion, was rather unsatisfactory, however. Particularly, the interesting series found in $NiBr_2$ between 16 434 and 17 300 cm^{-1}, partially due to exciton-magnon transitions, has stimulated further studies of magnetoabsorption[12] and neutron scattering[35] which have shed some light on the antiferromagnetic ordering of this compound. Nevertheless, the attribution of this transition to either $^1E(D)$, $^1T_1(D)$, or $^1A_1(G)$ was still in question. On the other hand, it is known that the halogen octahedral cage of $NiCl_2$ and NiI_2 is rather flattened [$u = 0.235$ and 0.233, respectively,[36] whereas the other $3d$-metal dihalides are considered in Wyckoff's book as undistorted, i.e., $u = 0.25$ (See Table III, Footnote a)].[37] A similar u value is expected for $NiBr_2$. Such a trigonal distortion is probably related to the relatively smaller ionic character of Ni dihalides, as will be shown in the next section. The combined effect of trigonal distortion and spin-orbit coupling on d^2 and d^8 crystal-field levels was recently investigated by KK.[11] Comparing the diagrams of Fig. 23, derived from KK calculations for the case $D\sigma = -D\tau$, with the general crystal-field spectra of Kozielski *et al.*[8] one can see that rather good agreement with the

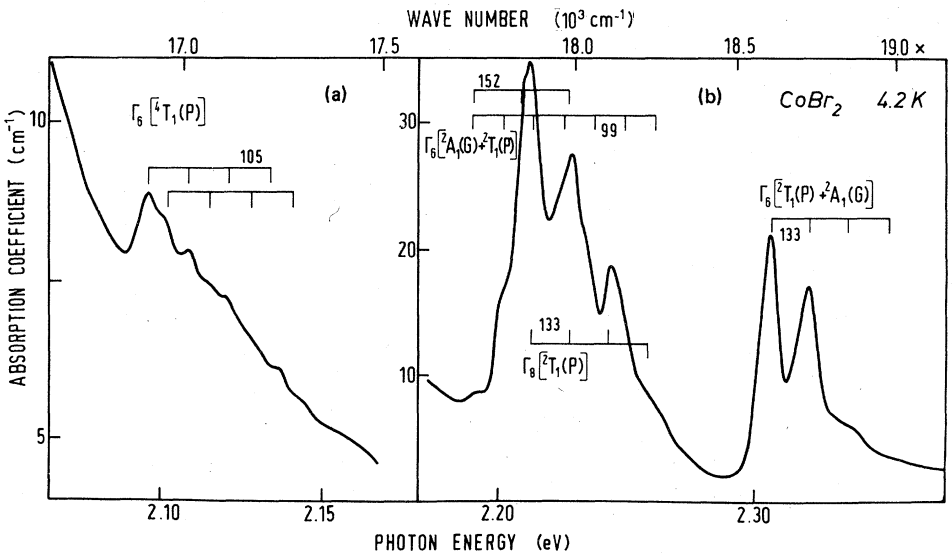

FIG. 18. Γ_6 component of the $^4T_1(P)$ band of $CoBr_2$ joined with the $^2A_1(G) + {}^2T_1(P)$ at 4.2 K.

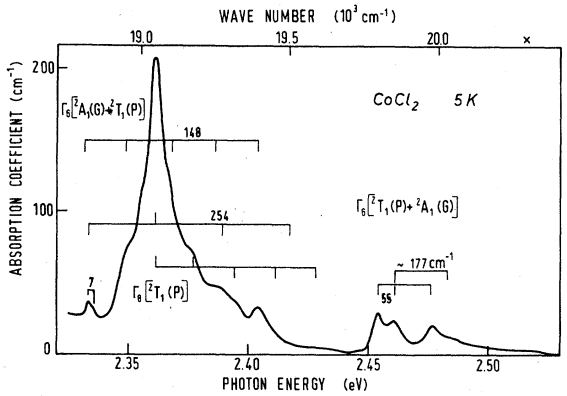

FIG. 19. $^2A_1(G)+{}^2T_1(P)$ bands in $CoCl_2$ at 5 K.

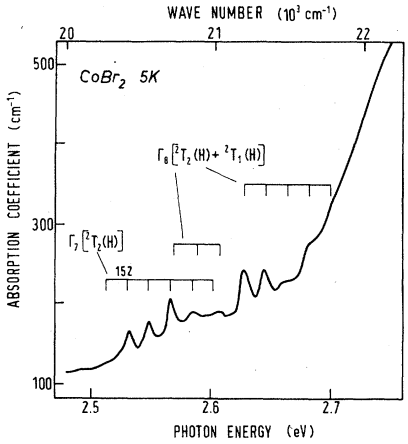

FIG. 21. $^2T_2(H)+{}^2T_1(H)$ bands of $CoBr_2$ at 5 K.

positions of the observed crystal-field transitions (spin-forbidden levels included) is obtained for both crystals when the trigonal-field corrections are included (see the vertical lines labeled $NiCl_2$ and $NiBr_2$ in Fig. 23). We have used the Racah parameters $B = 905$ cm^{-1} and $C = 4B$ as in KK[11] and the spin-orbit constant equal to -286 cm^{-1} for both crystals; $Dq = 757$ cm^{-1} and $D\tau = -153$ cm^{-1} for $NiCl_2$, $Dq = 846$ cm^{-1} and $D\tau = -290$ cm^{-1} for $NiBr_2$.

This fitting is now used to discuss the observed vibronic structures; we recall that the ground level is $^3A_2(F, e^2)$.

$^3T_2(F)$. The spin-orbit quartet (Γ_3, Γ_4, Γ_5, and Γ_2 in ascending order) is further split by the trigonal field into a lower group of four states (Γ_3^T, Γ_2^T, Γ_3^T, Γ_1^T, where index T denotes D_{3d} irreducible representations) corresponding to $^3E^T(F)$, and an upper nearly degenerate doublet (Γ_3^T and Γ_2^T) corresponding to $^3A_1^T(F)$. This is clearly seen in the experimental $^3T_2(F)$ band, where several progressions starting from *two distinct regions* can be recognized (Figs. 24 and 25). In $NiCl_2$ (Fig. 24), the first progressions of the subbands $^3E^T(F)$ and $^3A_1^T(F)$ start at $E_1 = 6519$ and $E_2 = 7407$ cm^{-1}, respectively. The sum of two Huang-Rhys functions

$$A_1 S_1^{n_1}/\Gamma(n_1+1) + A_2 S_2^{n_2}/\Gamma(n_2+1)\,, \tag{19}$$

where $n_i = (E - E_i)/\omega$, gives a reasonable fit of the whole $^3T_2(F)$ band with Huang-Rhys factors $S_1 = 3.5$ and $S_2 = 3.3$ and relative amplitudes $A_1 = 1.14$ and $A_2 = 0.65$, the phonon frequency $\bar{\omega}$ being set equal to 261 cm^{-1}.

We note that A_1 is approximately twice A_2. This is a further argument in favor of the present interpretation, according to which the separation of the two subbands is due to trigonal field rather than to spin-orbit interaction.[8]

The EC character of this transition suggests the attributing of the five phonon progressions, with a spacing of 261 cm^{-1} in $NiCl_2$ and 167 cm^{-1} in $NiBr_2$, to A_{1g} modes. These are in perfect agreement with the Raman frequencies (269 cm^{-1} for $NiCl_2$ and 168 cm^{-1} for $NiBr_2$; see Tables I and II).

$^3T_1(F) + {}^1E(D)$. Owing to the striking $E_g \times E_g$ two-phonon progressions associated with $^1E(D)$, these bands have been already published in detail in BPPT[10] (Ref. 10) and will not be reproduced. The bands associated with these levels are superimposed for the present values of Dq. In octahedral symmetry, mixing takes place via the Γ_3 components. In the trigonal field two additional Γ_3^T components come from the splitting of $^3T_1(F)$ into $^3A_2(F) + {}^3E^T(F)$, yielding more complicated hybridizations. However, the trigonal splitting produces also a large separation among $^3E^T(F)$, $^1E(D)$, and $^3A_2^T(F)$, so that $^1E(D)$ becomes quite isolated and very weakly dependent on both Dq and $D\tau$ (see Fig. 23). According to the theoretical introduction in Sec. II, the $^3A_2(F, e^2) - {}^1E(D, e^2)$ is then a candidate for

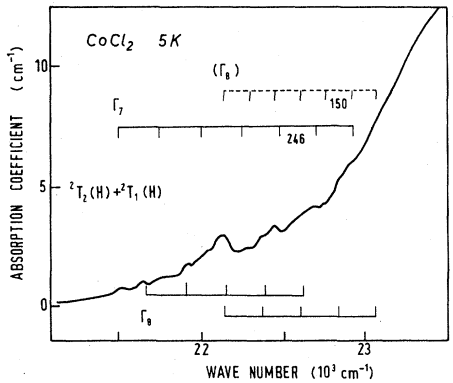

FIG. 20. $^2T_2(H)+{}^2T_1(H)$ band of $CoCl_2$ at 5 K.

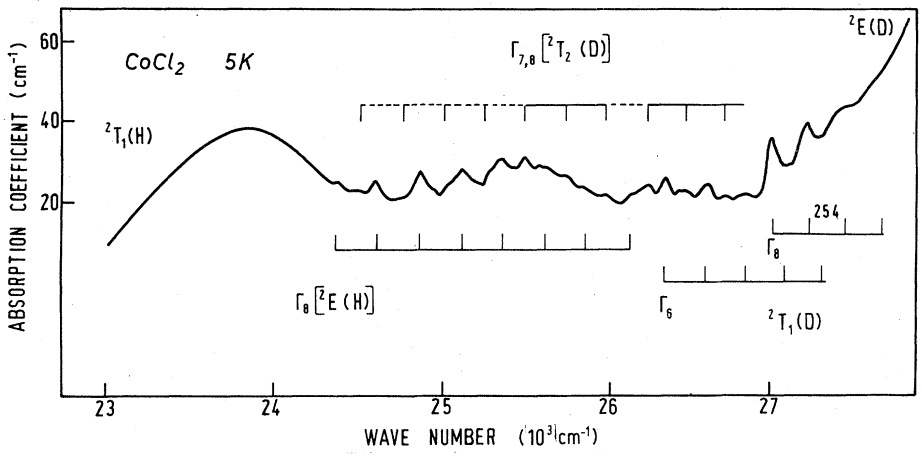

FIG. 22. $^2T_1(H)$, $^2E(H)$, and $^2T_1(D)$ bands of $CoCl_2$ at 5 K.

a two-phonon $E_g \times E_g$ progression. Indeed, the sharp progressions superimposed to the $^3T_1(F)$ band and starting from 13 300 cm^{-1} in $NiCl_2$ and 12 400 cm^{-1} in $NiBr_2$ have a spacing nearly twice the E_g Raman frequency (165 and 105 cm^{-1}, respectively) and are to date the best example of two-phonon vibronic structure originated by the second-order linear e-p interaction.[10]

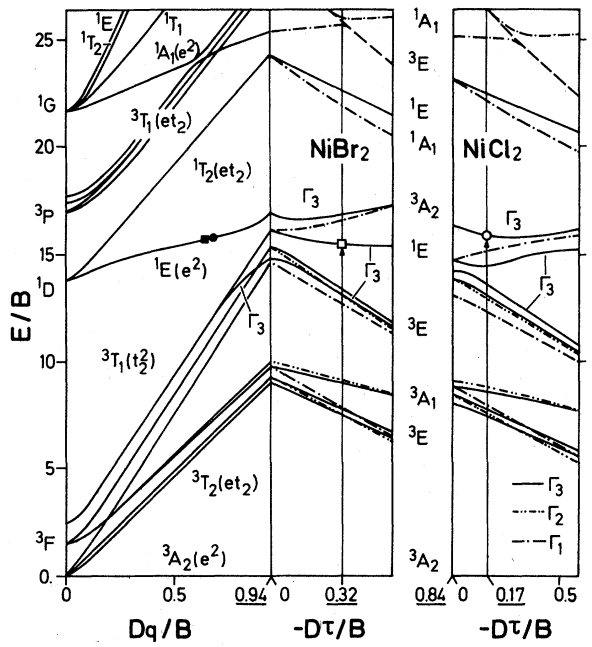

FIG. 23. Crystal-field levels of Ni^{2+} including spin-orbit interaction as functions of the cubic field (Dq) and of the trigonal field along the c axis for $D\sigma = -D\tau$. The black circle and square show the fitting of Dq/B (B = Racah parameter) to the position of ^1E (D) for $NiCl_2$ and $NiBr_2$, respectively, according to the attribution of Ref. 8, whereas the open circle and square correspond to the present fitting inclusive of the trigonal-field perturbation. The upper trigonal ^3E multiplet is schematically represented without structure (broken line).

It should be stressed that the vibronic analysis also provides a strong argument for assigning the sharp progressions appearing in the middle of the $^3T_1(F)$ band to $^1E(D)$. As concerns the "true" $^3T_1(F)$ transitions, we assign the two bands observed below $^1E(D)$ to $^3E^T(F)$ components and the broad weaker band found above $^1E(D)$ (not yet interpreted) to $^3A_2^T(F)$. Indeed, the spin-orbit quartet of $^3E^T(F)$ for $NiBr_2$ goes into two nearly degenerate doublets ($\Gamma_3^T + \Gamma_1^T$ and $\Gamma_3^T + \Gamma_2^T$) with a splitting on the order of 500 cm^{-1}, which may account for the net observation of a bump at 10 500 cm^{-1}; however, for $NiCl_2$ the calculated diagram predicts a triplet (Γ_1^T, the nearly degenerate $\Gamma_3^T + \Gamma_2^T$, and Γ_3^T). The strong EC character ($k = 2$) of $^3T_1(F)$ transitions is rather attenuated by the strong CM with the upper $^3T_1(P)$, and this may explain why a very weak corrugation corresponding to A_{1g} progressions has been observed in the band of $^3E^T(F)$ (see BPPT[10]).

$^1A_1(G) + {}^1T_2(D)$. The trigonal field splits $^1T_2$ into $^1A_1^T$ and $^1E^T$ and admixes this $^1A_1^T$ with the upper $^1A_1(G)$. For trigonal fields as large as that of $NiBr_2$, the two components of $^1T_2(D)$ are strongly lowered to the region between 16 400 and 17 200 cm^{-1} and split by ~800 cm^{-1}, while $^1A_1(G)$ is pushed up between the two trigonal components of the spin-allowed $^3T_1(P)$. In this case resolved phonon structures should be observed for $^1A_1^T(D)$ because of the large configuration mixing with $^1A_1(G)$, while the latter itself is undetectable. On the contrary, in $NiCl_2$ the splitting of $^1T_2(D)$ is small, the trigonal mixing with $^1A_1(G)$ is negligible, and $^1A_1(G)$ remains just above $^1T_2(D)$ but well below $^3T_1(P)$: In this case, if any structure is observed

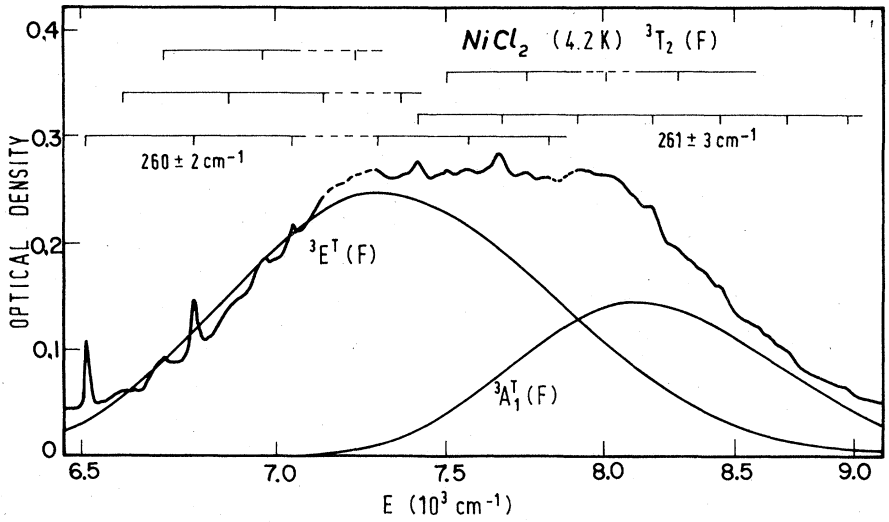

FIG. 24. $^3T_2(F)$ band in $NiCl_2$ at 4.2 K. We show also the calculated Huang-Rhys functions associated with the $^3E^T$ and $^4A_1^T$ subbands due to trigonal splittings.

in the region of $^1T_2(D)$, this is associated with $^1A_1(G)$. This analysis applies quite well to the observed spectra. Thus in $NiBr_2$ the structure around 16 500 cm^{-1}, earlier attributed to $^1E(D)$,[12] is definitely assigned to the spin-forbidden transition $^1T_2(D)$. We note that the magnetoabsorption analysis[12] interpreting the origins of this transition as due to magnon sidebands (exciton-magnon transitions) is still valid, being independent of the level assignment and is a good starting point for attempting a complete identification of the vibronic structure. With reference to Fig. 1 of Giordano *et al.*,[12] we note that an A_{1g} progression starting from 16 600 cm^{-1} and a pair of close E_g progressions, with a strong second-order character, starting from the two exciton-magnon lines can be proposed, while the stepwise series between 16 434 and 16 600 cm^{-1} could be an example of multimagnon sidebands of the type predicted by Bhandari and Falicov[37] and recently observed in luminescence spectra by Chiang *et al.*[38]

It is, however, difficult to accept these two origins at 16 600 and 16 434 cm^{-1} as due to the trigonal splitting of $^1T_2(D)$, since the latter is expected to be larger than 166 cm^{-1}. An alternative suggested interpretation could be the following. The broad

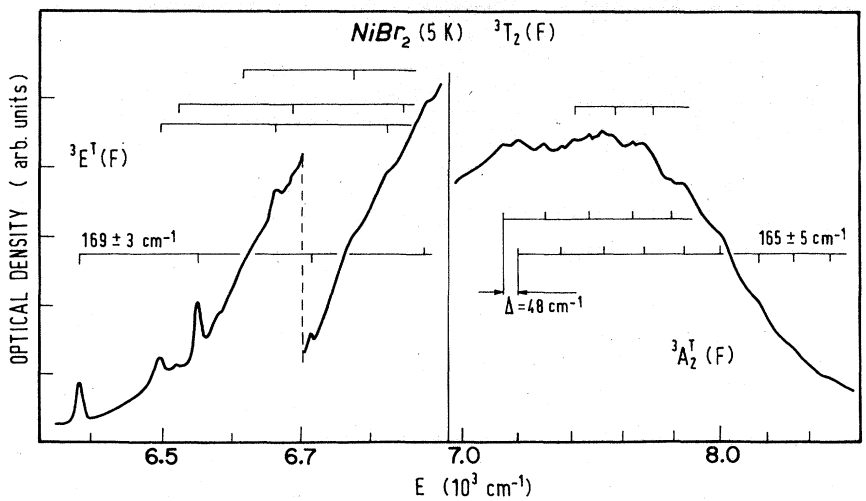

FIG. 25. $^3T_2(F)$ band in $NiBr_2$ at 4.2 K. Note that the two trigonal components are shown separately with different scales.

peak at 16 600 is an odd-phonon sideband [e.g., A_{2u} (TO) with $\omega = 230$ cm^{-1}, see below], as well as the two sharp peaks are magnon sidebands (with $\omega_M = 64$ and 72 cm^{-1}) of the *same* transition to the $^1A_1^T(D)$ singlet. The exciton-phonon transitions give obviously a much broader peak because of the broader dispersion of A_{2u} branch.[7] In this case we would shift up to 17 030 cm^{-1} the second origin [that corresponding to $^1E^T(D)$], obtaining a reasonable trigonal splitting of about 600 cm^{-1}.

In $NiCl_2$ the trigonal splitting of $^1T_2(D)$ and $^3T_1(P)$ is much smaller than in $NiBr_2$. Here the trigonal components $^1A_1^T(D)$ and $^1E^T(D)$ are practically superimposed, while $^1A_1(G)$ is expected to fall between $^1E^T(D)$ and the strong $^3T_1(P)$ band (whose trigonal splitting is now smaller than the multiphonon width). The weak progression affecting the shape of $^1T_2(D)$ and the left-hand side of $^3T_1(P)$ (Fig. 26) is therefore associated with the above $^1A_1$ transition. The spacing of 320 cm^{-1} coincides with that of $^1E(D)$ and is again assigned to an $E_g \times E_g$ two-phonon progression, in agreement with the IC nature of $^1A_1(G)$.

$^3T_1(P)$. The fitting by the inclusion of trigonal-field effects also implies a new assignment of this transition in $NiBr_2$. According to the diagram of Fig. 23, the two peaks at 19 800 and 22 200 cm^{-1} are just the two trigonal components of $^3T_1(P)$, namely, $^3A_2^T(P)$ and $^3E^T(P)$, respectively. The interpretation of the first band as being due to multimagnon processes earlier proposed on the basis of the observed temperature dependence[39] is not affected by this alternative assignment [$^3A_2^T(P)$ instead of $^1T_2(D)$]. However, by observing that around 19 800 cm^{-1}, we have in $NiBr_2$ the crossing and the mixing of $^1A_1(G)$ with $^3A_2^T(P)$, the large broadening of this peak for increasing temperature has another possible explanation: The change of D_T with temperature produces a relatively rapid separation of the two crossing levels, yielding a strong smearing of the band.

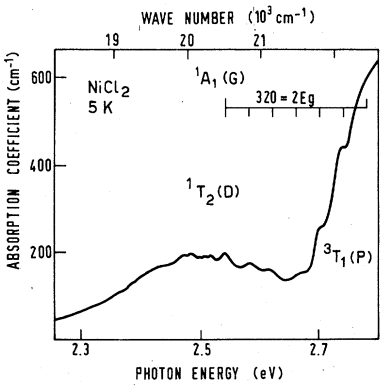

FIG. 26. $E_g \times E_g$ two-phonon progression of $^1A_1(G)$ transition superimposed to the $^1T_2(D)$ band in $NiCl_2$ at 5 K.

F. Far-infrared transmission data

The vibronic sidebands so far discussed have provided values of the A_{1g} and E_g optical modes. The information is completed by the far-infrared transmission data on powders, which give the TO frequencies of E_u and A_{2u} symmetries. The spectra obtained at $T = 300$ K are shown in Fig. 27 for all the crystals considered. The numbers labeling the peaks and the tails of the spectra give the transmission values in percent for each sample. The values of the frequencies $\omega(A_{2u}, \text{TO})$ and $\omega(E_u, \text{TO})$ are listed in Tables I (dichlorides) and II (dibromides). While the determination of $\omega(E_u, \text{TO})$ is relatively easy, that of $\omega(A_{2u}, \text{TO})$ presents some difficulty due to the weakness of the peak which can therefore be confused with that of the $E_g + E_u$ sideband (particularly in bromides) or with those of possible contaminants. Particularly in Co and Fe dihalides, the confidence in attributing the A_{2u} bump results from repeated measurements on several samples. In Fig. 27 the line corresponding to $E_u + E_g$ gives just the theoretical location of the combination band: Only in bromides does it correspond to small experimental peaks.

In $MnCl_2$ the structure at 235 cm^{-1}, previously attributed by Lockwood to E_u, TO, here is found to depend on the sample (contaminants) at least for the part above the broken line. On the other hand, the peak at 255 cm^{-1} is in good agreement with the recent neutron data (250 cm^{-1}).[40] The smallness of the A_{2u} peak and its dependence on the powder grain size leaves no doubt on this attribution and

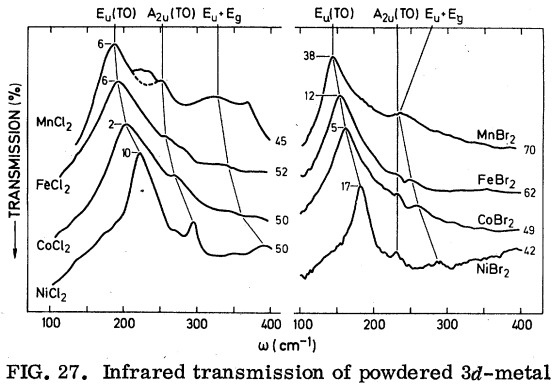

FIG. 27. Infrared transmission of powdered 3*d*-metal dihalides in nujol at 300 K. The transmission values at the E_u peak and at the high-frequency tail are indicated (in percent units and for a linear scale). The structure of $MnCl_2$ at 230 cm^{-1} is sample dependent (contaminants?); broken line shows the presumable intrinsic transmission. The line $E_u + E_g$ indicates the *theoretical* location of such a combination band.

on the fact that $\omega(A_{2u}, \mathrm{TO})$ is always above $\omega(E_u, \mathrm{TO})$ (unlike the earlier attribution of $MnCl_2$ and $CoCl_2$ frequencies by Lockwood[25]).

IV. DISCUSSION OF THE PHONON FREQUENCIES

The interpretative work so far presented is based to a large extent on general and qualitative arguments. A discussion of the vibronic structures starting from a microscopic calculation of the electron-phonon coupling and based on the comparison with calculated many-phonon band shapes would certainly be in order. This is, however, beyond our actual purpose (and our present capability). An aspect of this work which deserves further discussion is that concerning the phonon frequencies. The earlier misleading interpretations of the vibronic structures in Ni dihalides,[9] and also in MnI_2,[19] are examples of the importance of the preliminary knowledge of the optical vibrations. It is therefore useful to dispose of a simple dynamical model providing analytical expressions for the $\vec{q}=0$ optical frequencies in terms of few physical (and possibly known) parameters.

A. Model potential

When neutron dispersion curves and experimental elastic constants are not available (as for most of the present crystals), we may conveniently obtain information on the interionic potentials and force constants from the experimental cohesive energy and the equilibrium lattice configuration. However, when a crystal is only partially ionic, the cohesive energy is not a trivial concept as it depends on the definition of the dissociated phase. For consistency with the chosen interatomic potentials, the free ions of the gaseous phase must be prepared in the electronic configuration which is then kept unchanged during condensation. According to the procedure developed in Ref. 7, the cohesive energy $U(Z)$ turns out to be dependent on the fractional ionic charge Z because of covalency corrections to the metal ionization and halogen affinity potentials and other corrections due to the crystal-field stabilization and resonance energies. It is found that

$$U(Z)=U_0-I_1(1-Z)^2-I_2(1-Z^2)+A(2-Z-Z^2) - I_a Z(1-Z)-4\beta(1-Z^2)^{1/2}-E_S\,, \qquad (20)$$

where U_0 is the cohesive energy as given by the Born-Haber cycle for the ideal ionic case, I_1 and I_2 are the metal first- and second-ionization potentials, I_a and A are the halogen ionization and affinity energies, and E_S is the crystal-field stabilization energy.[41] The resonance energy β can be in turn related to some crystal macroscopic data as in Ref. 7, or simply by means of the Pauling-Sherman formula.[42] (The former procedure is used here.) $U(Z)$ is written as summation of interionic microscopic potential energies:

$$-U(Z)=6b_0e^{-r_0/\rho_0}+6be^{-a/\rho}+3be^{-a'/\rho} + 3be^{-a''/\rho}-\tilde{\alpha}_M Z^2e^2/r_0-S_6c_{dd}/a^6\,, \qquad (21)$$

where r_0 is the metal-halogen equilibrium distance. In nonideal (namely trigonally distorted) $C6$ and $C19$ structures we have three different distances between neighbor halogens: a (in the xy plane), a' (out of the xy plane, intralayer), and a'' (interlayer). For the halogen-halogen repulsive parameter b and ρ we use the values known for alkali halides.[43] The metal-halogen repulsive parameters b_0 and ρ_0 are fitted to the cohesive energy, once Z is known, and to the interionic distance r_0 via the equilibrium condition $\partial U(Z)/\partial r_0 = 0$.

The last term of Eq. (21) is the van der Waals interaction between halogen ions, where c_{dd} (derived from the approximate London formula[43]) takes the values 88×10^{-79} J m^6 for chlorides and 160×10^{-79} J m^6 for bromides.[7] The total Coulomb energy can be expressed via the effective Madelung constant $\tilde{\alpha}_M=\alpha_M+\Delta\alpha_M$, where α_M is the point ion Madelung constant and $\Delta\alpha_M$ the correction due to dipolar interaction.[36,7]

In the absence of trigonal distortion, the Madelung constant and the dipolar corrections practically take the same values in $C6$ and $C19$ structures,[44] so that Eq. (21) is valid for both lattice types. On the contrary, the Coulomb energy is quite sensitive to the trigonal distortion of the octahedral cage and to the deviation of the c-to-a ratio from the ideal value. Therefore the actual Madelung constant, calculated for each crystal, must be used.[7] On the other hand, the trigonal distortion has little effect on the halogen-halogen short-range terms (Born-Mayer and van der Waals terms give only a small contribution to the cohesion). Thus we set $a'=a''=a$. For the van der Waals lattice sum S_6, we use the value for the undistorted $C19$ structure $S_6=14.454$, which is just that for the fcc lattice.[43]

B. Optical frequencies

In the framework of deformation dipole model,[45] the four optical frequencies of a $C19$ structure, for $q\to0$ *along the c axis* and neglecting trigonal distortion, are given by

$$M_-\omega^2(A_{1g})=\frac{Z^{*2}e^2}{0.0976a^3+\alpha_-}+\frac{4b}{\rho^2}\left(2-\frac{\rho}{a}\right)e^{-a/\rho}-312\frac{c_{dd}}{a^8} + 2mZ^{*2}\frac{\mu_0 e}{a^4}+2nZ^{*2}\frac{\mu_0^2}{a^5}+\phi_r\,, \qquad (22)$$

$$M_-\omega^2(E_g)=\frac{-Z^{*2}e^2}{0.1959a^3-\alpha_-}+\frac{2b}{\rho^2}\left(1-\frac{5\rho}{a}\right)e^{-a/\rho}-24\frac{c_{dd}}{a^8}$$
$$-mZ^{*2}\frac{\mu_0 e}{a^4}-nZ^{*2}\frac{\mu_0^2}{a^5}+\phi_r\,, \tag{23}$$

$$\mu\omega_L^2(A_{2u})=\frac{Z^{*2}e^2}{0.0841a^3+\alpha}+2mZ^{*2}\frac{\mu_0 e}{a^4}+\phi_r\,, \tag{24}$$

$$\mu\omega_T^2(E_u)=\frac{-Z^{*2}e^2}{0.1690a^3-\alpha}-mZ^{*2}\frac{\mu_0 e}{a^4}+\phi_r\,, \tag{25}$$

where M_- and $\mu=M_+M_-/(M_++2M_-)$ are the halogen and the reduced mass, respectively, $2\alpha\equiv\alpha_++2\alpha_-$ is the cell polarizability, and Z^*e is the Szigeti effective charge. Since, in absence of trigonal distortion, the halogen sublattice is fcc, the above expressions are readily obtained by observing that

(i) A_{1g} and E_g Coulomb and van der Waals terms are formally equal to force constants of a rocksalt crystal at the L point;

(ii) A_{2u} and E_u Coulomb terms correspond to rocksalt force constants at the Γ point.[46]

The dimensionless lattice sums $m=34.03$ and $n=-126.8$ for the metal-halogen pole-dipole interaction and halogen-halogen dipole-dipole interaction, respectively, are taken from the van der Valk and Haas work as well as the expression for the static dipole μ_0.[47] Furthermore,

$$\phi_r=\frac{b_0}{\rho_0^2}\left(1-\frac{2\rho_0}{r_0}\right)e^{-r_0/\rho_0} \tag{26}$$

is the metal-halogen repulsive force constant.[48]

We note that the fitted metal-halogen short-range term incorporates in some way the *two-body* effects of covalency. However, covalency may contribute also non-negligible three-body nearest-neighbor terms which cannot be surrogated by any short-range two-body force constant. In fact they induce anisotropy between A_{1g} and E_g modes and between even- and odd-symmetry modes, whereas the two-body force constants do not.[49,50] Therefore in the following discussion the theoretical expressions of the $q=0$ phonon frequencies shall also include, as additional contributions, some typical valence field terms, such as the angle-bending force constants ϕ_θ and $\phi_{r\theta}$ for each halogen-metal-halogen triad forming a right angle.[49-51] In this case a three-body contribution ϕ_{3b} given by

$$\phi_{3b}(A_{1g})=8\phi_\theta\,, \tag{27}$$

$$\phi_{3b}(E_g)=2\phi_\theta\,, \tag{27'}$$

$$\phi_{3b}(A_{2u})=\phi_{3b}(E_u)=4\phi_\theta-8\phi_{r\theta}\,, \tag{27''}$$

TABLE III. Input crystal data, effective and net charges, repulsive parameters, and nearest-neighbor two-body and three-body force constants.

	a [a] (Å)	α_M [b] (1)	$-U_0$ (10^{-19} J/mol)	α_+ [c] (Å^3)	Z^* (e)	Z (e)	ρ_0 (Å)	$\ln\frac{b_0}{10^{-19}\,\mathrm{J}}$	ϕ_r	$8\phi_\theta$ (kg s^{-1})	$\phi_{\theta r}$
$MnCl_2$	3.686	4.414	41.51	0.48	0.50	0.91	0.3293	7.654	51.05		
						0.88	0.3816	6.662	40.22	4.99	1.27
$FeCl_2$	3.579	4.365	43.13	0.46	0.42	0.85	0.3028	7.907	52.92		
						0.80	0.3766	6.387	33.77	4.28	0.21
$CoCl_2$	3.544	4.359	44.13	0.56	0.41	0.79	0.2664	8.678	55.01		
						0.75	0.3111	7.395	40.59	6.09	1.32
$NiCl_2$	3.543	4.435	45.73	0.66	0.40	0.72	0.2008	11.350	67.45		
						0.68	0.2429	9.267	46.40	6.39	0.00
$MnBr_2$	3.820	4.378	40.12	0.48	0.50	0.92	0.3564	7.272	42.84		
						0.91	0.3808	6.839	38.18	3.30	0.93
$FeBr_2$	3.772	4.348	42.02	0.46	0.51	0.83	0.2815	8.749	48.16		
						0.82	0.2993	8.227	44.47	2.47	0.47
$CoBr_2$	3.728	4.333	42.97	0.56	0.40	0.78	0.2330	10.236	51.58		
						0.77	0.2488	9.558	45.14	3.37	1.25
$NiBr_2$	3.708	4.439	44.65	0.66	0.35	0.73	0.2149	10.974	53.02		
						0.70	0.2604	8.951	39.45	5.02	1.07

$\alpha_-(Cl^-)=2.974$ Å^3 [d] $\quad\alpha_-(Br^-)=4.130$ Å^3 [d] $\quad\rho=0.3394$ Å [f] $\quad\ln\frac{b(Cl^-)}{10^{-19}\,\mathrm{J}}=7.818$ [f] $\quad\ln\frac{b(Br^-)}{10^{-19}\,\mathrm{J}}=8.571$ [f]

$c_{dd}(Cl^-)=88\times10^{-79}$ J m^6 [e] $\quad c_{dd}(Br^-)=160\times10^{-79}$ J m^6 [e]

[a] R. W. G. Wyckoff, *Crystal Structures* (Interscience, New York, 1972), Vol. 1.
[b] Reference 7.
[c] J. Shanker and M. P. Verma, J. Phys. Chem. Solids 17, 639 (1976).
[d] J. R. Tessman, A. H. Kahn, and W. Shockley, Phys. Rev. 92, 890 (1953).
[e] Average values over the series from Cr to Ni halides (see Ref. 7).
[f] Reference 43.

is added to the nearest-neighbor force constant ϕ_r,

First we calculate the optical frequencies in the two-body approximation. In this case the only disposable parameters are Z and Z^*. They are obtained by a best fit of the four experimental frequencies reported in Table III.

Furthermore, the calculated longitudinal A_{2u} frequency may be significantly larger than the experimental transverse A_{2u} frequency obtained from infrared absorption. In this kind of material, however, the LO-TO splitting of the A_{2u} mode is usually small compared with the A_{2u} frequency itself (less than 7%), because of a compensation mechanism of the dynamical anisotropy by the dipolar forces.[49,7,52,53] The fitted values of Z and Z^* and the corresponding ρ_0, b_0, and ϕ_r are displayed in Table III, first row for each crystal, with other crystal data.

The force constants which are directly calculated from crystal data, namely the Coulomb (ϕ_C), dipolar (ϕ_d), halogen-halogen repulsive (ϕ_{2n}) and van der Waals (ϕ_{vdW}) force constants are listed in Table I, together with the calculated frequencies. We see that the agreement with the experimental frequencies is rather good for all crystals. Furthermore we obtain a quite reasonable *scale of ionicity*, ranging from more than 90% for Mn dihalides to less than 75% for Ni dihalides. These ionicity values are in the same range as those required in the crystal-field calculation by Stout[54] (0.87 for $MnCl_2$ and 0.85 for $MnBr_2$) and are consistent with the calculated free molecule ionicities,[42] also decreasing from $MnCl_2$ ($x = 0.79$) to $NiCl_2$ ($x = 0.69$). Particularly, the enhanced covalency of Ni dihalides is in line with the conclusions of Wilson and Joffe,[55] who predict for these crystals a metal-insulator transition.

The partial covalency of these crystals might result in the existence of non-negligible three-body force constants like those introduced in our model. In order to have an idea on how large are the three-body terms, we have performed an exact fitting of the four experimental frequencies adding to Z^* and Z the two unknown additional parameters ϕ_θ and $\phi_{r\theta}$. The results of this second fitting procedure are shown in Table III, second row for each crystal. We note that the most important contribution comes from ϕ_θ, whereas $\phi_{r\theta}$ is rather small, and ϕ_θ increases from Mn to Ni dihalides, in agreement with the behavior of covalency.

ACKNOWLEDGMENTS

The authors would like to thank the Istituto di Chimica delle Macromolecole, Consiglio Nazionale delle Ricerche, Milano, for allowing the use of the far-infrared spectrophotometer. One of us (G.B.) acknowledges Professor Heinz Bilz and Dr. Axel Frey for several stimulating discussions during his stay at the Max-Planck-Institut Für Festkörperforschung of Stuttgart.

*Permanent address.
[1]S. Sugano, Y. Tanabe, and H. Kamimura, *Multiplets of Transition Metal Ions in Crystals* (Academic, New York, 1970).
[2]R. Englman, *The Jahn-Teller Effect in Molecules and Crystals* (Wiley, New York, 1972).
[3]Yu. E. Perlin and B. S. Tsukerblat, *Effekty elektron-nokolebatel' nogo vzaimodeistviya v opticheskikh spektrakh primesnykh paramagnitinykh ionov* (Shtiintsa, Kishinev, 1974).
[4]A. Abragam and B. Bleaney, *Electron Paramagnetic Resonance of Transition Ions* (Oxford University Press, New York, 1970), Vol. II, Chap. 21.
[5]I. W. Johnstone, D. J. Lockwood, and G. Mischler, J. Phys. C 11, 2147 (1978).
[6]A. Pasternak, J. Phys. C 9, 2987 (1976).
[7]G. Benedek and A. Frey, Phys. Rev. 21, 2482 (1980).
[8]M. Kozielski, I. Pollini, and G. Spinolo, J. Phys. C 5, 1253 (1972).
[9]G. Benedek, I. Pollini, and G. Spinolo in, *Proceedings of the International Conference on Lattice Dynamics, Paris, 1977,* edited by M. Balkanski (Flammarion, Paris, 1978), p. 68.
[10]G. Benedek, I. Pollini, L. Piseri, and R. Tubino (BPPT), Phys. Rev. B 20, 4303 (1979).
[11]E. König and S. Kremer, *Ligand Field Energy Diagrams* (Plenum, New York, 1977).
[12]P. Giordano, I. Pollini, L. Reatto, and G. Spinolo, Phys. Rev. B 17, 257 (1978).
[13]A. A. Maradudin and R. F. Wallis, Phys. Rev. 123, 777 (1961). See also A. A. Maradudin, Solid State Phys. 19, 1 (1967).
[14]H. Sumi, J. Phys. Soc. Jpn. 36, 770 (1974); 38, 825 (1975).
[15]E. Mulazzi, G. F. Nardelli, and N. Terzi, Phys. Rev. 172, 847 (1968).
[16]A. A. Maradudin, Solid State Phys. 18, 399 (1966).
[17]M. A. Krivoglatz, Fiz. Tverd. Tela (Leningrad) 6, 1707 (1964) [Sov. Phys.— Solid State 6, 1340 (1964)].
[18]Yu. B. Rozenfel'd and V. Z. Polinger, Zh. Eksp. Teor. Fiz. 70, 597 (1976) [Sov. Phys.—JETP 43, 310 (1976)].
[19]J. van Erk, Ph.D. thesis, University of Groningen, 1974 (unpublished).
[20]J. van Erk and C. Haas, Phys. Status Solidi B 70, 517 (1975).
[21]M. H. L. Pryce, in *Phonons and Phonon Interaction* edited by H. Stevenson (Plenum, New York, 1966), p. 403.
[22]P. Pappalardo, J. Chem. Phys. 31, 1050 (1959).
[23]P. Pappalardo, J. Chem. Phys. 33, 613 (1960).
[24]L. Orgel, J. Chem. Phys. 23, 1004 (1955).
[25]D. J. Lockwood, J. Opt. Soc. Am. 63, 374 (1973).

[26]D. D. Sell, R. L. Green, and R. M. White, Phys. Rev. 158, 489 (1967).
[27]G. Güntherodt, W. Bauhofer, and G. Benedek, Phys. Rev. Lett. 43, 1427 (1979).
[28]D. J. Robbins and P. Day, J. Phys. C 9, 867 (1976); E. Wood, A. Muirhead, and P. Day, *ibid.* 11, 1619 (1978).
[29]S. E. Schnatterly and M. Fontana, J. Phys. (Paris) 33, 691 (1972) for $FeCl_2$ and J. A. Griffin and J. D. Litster, AIP Conf. Proc. 29, 652 (1976) for $FeBr_2$.
[30]I. Pollini and G. Spinolo, Phys. Lett. 72A, 261 (1979).
[31]E. König and S. Kremer, J. Phys. Chem. 78, 56 (1974).
[32]J. Ferguson, D. L. Wood, and K. Knox, J. Chem. Phys. 39, 881 (1963).
[33]A. D. Liehr, J. Phys. Chem. 67, 1314 (1963).
[34]A. D. Liehr, and C. J. Ballhausen, Ann. Phys. (NY) 2, 134 (1959).
[35]P. Day, A. Dinsdale, E. R. Krausz, and D. J. Robbins, J. Phys. C 9, 2481 (1976).
[36]Y. M. de Haan, in *Molecular Dynamics and Structure of Solids*, edited by R. S. Carter and J. J. Rush (Natl. Bur. Stand., Washington, 1969) [Natl. Bur. Stand. (U.S.), Spec. Publ. 301, (1969)], p. 233.
[37]R. Bhandari and L. M. Falicov, J. Phys. C 5, 1445 (1972).
[38]T. C. Chiang, P. Salvi, J. Davies, and Y. R. Shen, Solid State Commun. 26, 217 (1978).
[39]M. Kozielski, I. Pollini, and G. Spinolo, Phys. Rev. Lett. 27, 1223 (1971).
[40]C. Escribe, J. Bouillot, and K. R. A. Ziebeck, J. Phys. C 13, 4053 (1980).
[41]D. S. McClure, in *Phonons and Phonon Interactions*, edited by H. Stevenson (Plenum, New York, 1966), p. 314.
[42]R. G. Pearson and H. B. Gray, Inorg. Chem. 2, 358 (1963).
[43]M. P. Tosi, Solid State Phys. 16, 1 (1964).
[44]E. Lombardi and L. Jensen, Phys. Rev. 151, 694 (1966).
[45]J. R. Hardy, Philos. Mag. 7, 315 (1962). For a discussion of the model and a critical comparison with the shell models see the recent book by H. Bilz and W. Kress *Phonon Dispersion Relations in Insulators* (Springer, Berlin, 1979).
[46]Obviously the expression of the rocksalt dynamical matrix in the deformation dipole model is considered to be well known, e.g., from Ref. 45.
[47]H. J. L. van der Valk and C. Haas, Phys. Status Solidi B 80, 321 (1977).
[48]The above equations represent also a good approximation for the frequencies of CdI_2 ($C6$) structure. With respect to $CdCl_2$ ($C19$) structure, all CdI_2 intralayer force constants have the same expression, while the Coulomb force constants are only slightly modified. Recently, careful lattice-dynamical calculations for $C6$ structures, with application to PbI_2, have been performed by A. Frey, Ph.D. thesis, University of Stuttgart, 1977 (unpublished), who has taken into account also the trigonal distortion. [A short account is given in A. Frey and R. Zeyher, Solid State Commun. 28, 435 (1978).] In this work the numerical factors occurring in the denominator of the Coulomb force constants, for the specific case of PbI_2 are 0.1027, 0.2049, 0.0909, and 0.1642 for A_{1g}, E_g, A_{2u} (LO), and E_u(TO) modes respectively. These values differ from those for the ideal $CdCl_2$ structure, appearing in Eqs. (22)–(25), only by 3% to 7%. Since the maximum contribution of the Coulomb term is usually not larger than 15% of the total force constant, Eqs. (22)–(25) are seen to give also the frequencies of $C6$ lattices within less than 0.5%. Therefore they can be conveniently used for both $C6$ and $C19$ structures.
[49]G. Lukowski and R. M. White, Nuovo Cimento 38B, 290 (1977).
[50]G. Lukowski, J. C. Minkelsen, W. Y. Liang, R. M. White, and R. M. Martin, Phys. Rev. B 14, 1663 (1978).
[51]J. C. Phillips, *Covalent Bonding in Crystals, Molecules and Polymers* (University of Chicago Press, Chicago, 1969), p. 203.
[52]A. Frey and R. Zeyher, Solid State Commun. 28, 435 (1978).
[53]A. Frey and G. Benedek, Solid State Commun. 32, 305 (1979).
[54]J. W. Stout, J. Chem. Phys. 33, 303 (1960).
[55]J. A. Wilson and A. D. Yoffe, Adv. Phys. 18, 193 (1974).